Chapter 4

Synthesis and characterization of Fe, Ni (dual Metal-Metal) doped ZnS NPs and their photocatalytic activity

4.1 Introduction

When the whole world has attention to renewable energy source and resources to utilize them efficiently, the role of photovoltaic and photocatalytic materials dominates the regime. Zinc Sulphide, a polymorphic compound of II-VI semiconductor class, with zinc blende (ZB) and wurtzite (WZ) as major phases presents itself for both photocatalytic and photovoltaic properties based on its dispersed/flat conduction/valence band that signifies a low recombination rate of charge carriers. While its wide bandgap can accommodate large dopants required to create recombination or trapping sites for charge separation. ZB is found energetically and physically more stable while WZ is a higher temperature phase, vast investigations on ZnS-ZB have been performed for its electronic, optical, catalytic, magnetic, and spintronic applications but lack of visible light absorption, small surface area, and low reusable capacity have kept it at a distance from commercialization.

In the environment, there are various pollution-related issues like water adulteration, industrial air pollution, and global warming, which adversely affect biodiversity. Over the last few years, due to industrialization and urbanization, water quality is continuously falling. The main pollutants of this pollution are organic dyes, pigments, and inks. They relay a negative impact on the environment, which in turn affects human health, so elimination of these pollutants is necessary because most of the dyes and their breakdown products are toxic, carcinogenic, or mutagenic. To overcome these difficulties, several cost-effective techniques were proposed in the last few years. The removal of these hazardous dyes and contaminants from the aqueous environment has become a challenging chore.

Hence, numerous strategies have been developed to deal with these specific problems such as ion exchange removal[1], ozonation[2], bioadsorption[3], adsorption[4], catalytic reduction[5], aerobic treatment [6], and coagulation[7]. The issues like the incomplete removal of contaminants, low absorption efficiency, and meager mechanical stability of adsorbents create problems for the effective removal of pollutants[8]. The photodegradation of contaminants has gained enormous approval in the past several years.[9–11] The photocatalytic reaction includes heterogeneous catalysis, where a semiconductor photocatalyst absorbs sunlight to destroy various aquatic and atmospheric organic contaminants. Photodegradation using semiconductor NCs provides

solution over the traditional wastewater treatment methods because the whole degradation of organic pollutants by active photocatalysts can occur within a few hours at room temperature. Moreover, by using semiconductor NCs, the formation of the secondary toxic products can be entirely mineralized into relatively non-hazardous products (i.e.water and CO_2).[12,13] The whole photodegradation procedure, from the adsorption of dye molecules on the photocatalyst surface to the decomposition of dye molecules by reactive radicals, is influenced by several operational parameters, such as the initial dye concentration, pH of the solution, irradiation intensity, and reaction temperature.[14–17] Fujishima and Honda developed the phenomenon of a photocatalytic splitting of water using UV light on TiO_2 electrode in 1972.[18] Folli et al established TiO_2 surface chemistry for its photocatalytic performances. Nowdays, the research work focused on the dispersion and aggregation properties of commercially available titania for their application as photocatalysts. Thus, photocatalytic degradation of pollutants by using semiconductor nanoparticles is the area of research that captured great attention to solve environment related problems. The physical properties of semiconducting materials can be altered at nano sizes and shapes due to quantum confinement effects.

Metal sulfides semiconductor play an important role as photocatalyst as in metal sulfides the less positive valance band occupied by S 3p orbitals and small effective mass carriers permit metal sulfides to generate appropriate energy band structure, and fast charge carrier dynamics with extensive photoresponse range, which leads to the high photocatalytic conversion efficiency like conversion of CO_2 into great value-added chemicals. Metal sulfides having one or more metal elements are usually classified as binary metal sulfides (CdS, ZnS, etc.), ternary metal sulfides ($ZnIn_2S_4$, $CuInS_2$, etc.), and polyary metal sulfides (Cu_2ZnSnS_4, etc.) according to the elemental composition.[19]

The photocatalytic removal of toxic compounds like phenolic compounds, dyes, pesticides, etc. using the photoactive materials mainly depends on the amount of catalyst, the bandgap, surface area to volume ratio, and generation of an electron-hole pair. The bandgap can be tuned by introducing dopants ion, particularly from transition metal or lanthanide groups. Judiciously selected dopant ions add extra energy levels between the VB and the CB of the host[20]. Various types of semiconductors have been used for this purpose in the last decades, among them metal chalcogenides NPS emerge as a new class of active materials for dye removal. Recently B. Sreenivasulu et al have published optical and magnetic properties of (Cu, Ni), (Co, Ni), and (Fe, Ni) co-doped ZnS nanoparticles.[21,22] To the best of our knowledge there is no report on photocatalytic degradation and electrochemical properties for (Fe, Ni) co-doped ZnS.

In present work, a simple co-precipitation method was used for the synthesis of Fe doped and Ni co-doped 2-mercaptoethanol capped ZnS NPS. The influence of different concentrations of dopants on the structural, optical, electrical, magnetic, and electrochemical properties were studied in detail.

The role of transition metal (TM) and non-metal interaction in terms of p_{π}-d_{π} coupling over rapid charge migration, reduced rate of recombination, increased optical absorbance, and formation of charge trapping sites boost the photocatalytic efficiency exponentially. Inclusion of TM induces ferromagnetic property leading to its utilization as a reusable photocatalyst increasing its life cycle for better dye degradation and water splitting ability. We have also carried out theoretical study on Fe, Ni mono and co-doped ZnS system by emphasizing on band edge straddling, large variance in the effective mass of photo-generated electron-hole pair and presence of intermediate states due to the trapping of excitons, these reduce the recovery time to enhance the photo activity of the free surface.

4.2 Synthesis of the catalysts

Materials and Methods

Zinc acetate dihydrate $(CH_3COO)_2Zn.2H_2O$) AR grade sigma Aldrich, Ferrous tetrachloride tetrahydrate ($FeCl_2.4H_2O$) AR grade Merck, Nickel acetate tetrahydrate ($(CH_3COO)_2Ni.4H_2O$) AR grade Merck were used for doping. Sodium hydroxide (NaOH) AR grade Merck, Sodium sulfide ($Na_2S.xH_2O$) AR grade Loba Chemie, 2-Mercaptoehanol ($HSCH_2CH_2OH$) AR grade sigma Aldrich, RhodamineB ($C_{28}H_{31}ClN_2O_3$) S.D. Fine Chemicals. All reagents were used without any further purification. 2-Mercaptoethanol was used as a capping agent. In a typical procedure,[23] 5×10^{-3} mol of Zinc acetate was dissolved in 200 ml D.I water. 50 ml of each dopant (11.49×10^{-5}mol, for $Fe_{0.07}$ and 9.18×10^{-5}mol, for $Ni_{0.07}$) and ferrous chloride (8.19×10^{-5}mol, $Fe_{0.05}$ and 6.56×10^{-5}, for $Ni_{0.05}$) were added dropwise under vigorous stirring. Stirring was continued for 40 min until complete dissolution of both dopants. During the experiment, the pH of the solution was maintained at 11 using an aqueous solution of NaOH (1M), followed by dropwise addition of 2-mercaptoethanol (0.025mol in 50ml). The temperature of the reaction mixture was gradually raised to 70°C. The reaction mixture was stirred thoroughly for further half an hour to obtain a homogenous mixture. To this Na_2S solution, (5×10^{-3}mol in 50 ml) was added dropwise at the rate of 1mL /min. The reaction mixture was further stirred for 3hr to obtain homogenous stabilized dispersion and then allowed to cool naturally. The mixture was centrifuged at 6000 rpm for 5 min and washed with DI water

4 times and finally with absolute alcohol to remove impurities. The resulting precipitate was dried at 60°C. The color of ZnS: Fe: Ni co-doped samples was brown. Pristine ZnS was also synthesized by the same method without using dopants (Fig. 4.1).

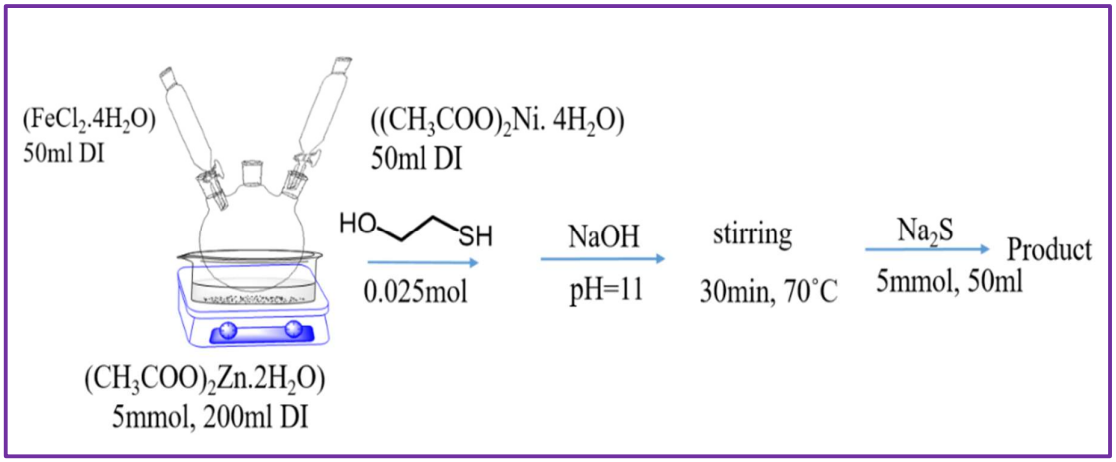

Fig. 4.1. Schematic procedure for the synthesis of Fe, Ni co-doped ZnS Nps.

Table 4.1 Composition of dopants.

Dopants(%)	**$((CH_3COO)_2Ni.\ 4H_2O)$**	**$(FeCl_2.4H_2O)$**
$Zn_{1-0.14}Fe_{0.07}Ni_{0.07}S$	9.18×10^{-5}mol	11.49×10^{-5}mol
$Zn_{1-0.10}Fe_{0.05}\ Ni_{0.05}S$	6.56×10^{-5}mol	8.19×10^{-5}mol
$Zn_{1-0.07}Fe_{0.07}S$	-	11.49×10^{-5}mol
$Zn_{1-0.05}Fe_{0.05}S$	-	8.19×10^{-5}mol
$Zn_{1-0.07}Ni_{0.07}S$	9.18×10^{-5}mol	-
$Zn_{1-0.05}Ni_{0.05}S$	6.56×10^{-5}mol	-
Pristine	-	-

4.3 Characterization

X-Ray powder sample diffraction(XRD) patterns of samples were obtained by X-ray Diffractometer (Panalytical X Pert Pro) with Cu Kα radiation, λ= 0.15418nm,100 kV. Transmission electron microscopy (TEM) is carried out using JEOL JSM-2100 Microscope and Scanning electron microscopy (Nova nanoSEM 450) were employed to confirm the size and morphology of the nanoparticles. Uv-Visible spectra were recorded on PerkinElmer

Lambda 35, while photo-luminescence spectra were recorded on Jasco FP-6300 at RT. Photoluminescence (PL) spectra were recorded using a Xenon lamp as the excitation source at 290 nm. The samples were degassed at 80°C preceding to Brunauer-Emmett-Teller(BET) measurements. The BET surface area (SBET) was calculated by nitrogen adsorption (Micrometrics ASAP 2020, USA) via a multipoint BET method using the adsorption data in the relative(P/P_o) range of 0.0-1.0. The porosity of prepared samples was evaluated by desorption isotherms using the Barret-Joyner-Halender (BJH) method.

Chemical composition analysis of all the samples was done by the EDAX technique (JEOL 8086). SEM Images with elemental Mapping were performed using a Gold grid. Vibrating sample magnetometer (VSM) analysis was carried out for the study of the magnetic behavior of synthesized samples at room temperature under applied magnetic fields up to 15000Oe on Lakeshore, Model:7410 series.

The Hydrodynamic size of Nanoparticles was calculated using a BIC 90 plus (Brookhaven), equipped with 35.0mW solid-state lasers operating at 660 nm, and Surface charge (Zeta potential) measurement was carried out using an avalanche photodiode detector. Nanoparticle film, calomel, and Pt wire were taken as working electrodes, reference, and counter electrodes respectively in 0.1 M KCl solution. Donar density was calculated using the given formula.

Calculation of donor density (N_D)

$$N_D = \frac{2}{\varepsilon.\varepsilon_0.A^2.e.slope}$$

Where, ε_0 = Dielectric constant of vacuum (8.85 x 10^{-14}F cm^{-1})

ε = Dielectric constant of ZnS materials(8.50)

A^2= Area of electrode (1 cm^2)

e = electron charge (1.60 x 10^{-19} C)

4.4 Result and Discussion

The XRD pattern of all synthesized co-doped ZnS NPs manifests three predominant diffraction peaks corresponding to the (111), (220), and (311) planes respectively which are in good agreement with the standard diffraction peaks (JCPDS 00-001-0792) of cubic structure (Fig. 4.2 (A)). These results suggested clearly that the doping does not affect the crystal structure significantly. A broad peak corresponded to (111) planes in the case of co-doped $Zn_{1.0.14}Fe_{0.07}Ni_{0.07}S$ (Fig. 4.2A (a)) and $Zn_{1.07}Fe_{0.07}S$ became distorted (Fig. 4.2A (c)).

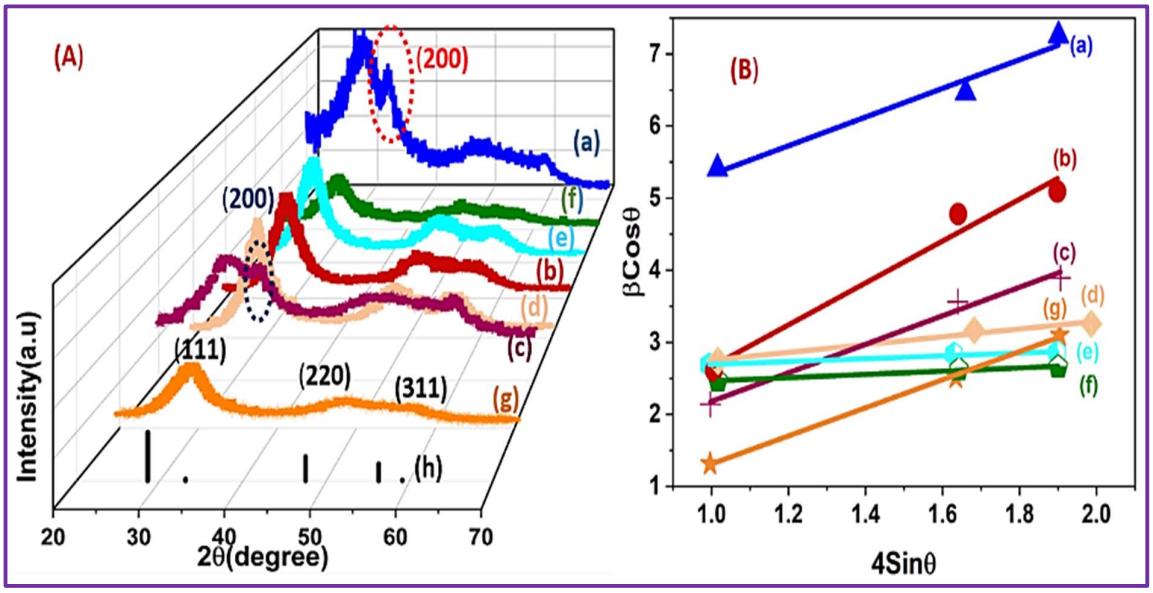

Fig. 4.2. (A) PXRD of ZnS (a) $Zn_{1-0.14}Fe_{0.07}Ni_{0.07}S$ (b) $Zn_{1-0.10}Fe_{0.05}Ni_{0.05}S$ (c) $Zn_{1-0.07}Fe_{0.07}S$ (d) $Zn_{1-0.05}Fe_{0.05}S$ (e) $Zn_{1-0.07}Ni_{0.07}S$ (f) $Zn_{1-0.05}Ni_{0.05}$ (g) Pristine (h) Bulk JCPDS card 00-005-0566Z. (B) W-H plot.

This kind of distortion indicates the phase change in ZnS host lattice from cubic to wurtzite. The mean crystallite size of nanoparticles was calculated using the Debye-Scherrer equation (Eq. (1)), as per the formula[24]

$$D = \frac{0.94\lambda}{\beta cos\theta} \quad (1)$$

where, D is the crystallite size, λ is the wavelength of X-Rays (1.54056A°), β is the full width at the half maxima (in rad) and θ is the Bragg's angle. The broadening in peaks could be due to the lattice strain (ε) and stress. The lattice strain was estimated by Stokes and Wilson equation (Eq. (2))

$$\varepsilon = \frac{\beta}{4tan\theta} \quad (2)$$

In addition to the Scherrer equation, the average lattice strains and particle size (Table1) for all the synthesized ZnS NPs were calculated by the Williamson-Hall (W-H) method[25] (Eq.(3))

$$\beta cos\theta = \frac{\kappa\lambda}{D} + 4\varepsilon\, sin\theta \quad (3)$$

The plot βcosθ vs 4sinθ gives a positive straight line indicating the tensile strain of the synthesized NPs, lattice strains of the synthesized NPs were estimated from the slope of this

graph, while the average crystallite size was calculated from the y-intercept of this straight line by fitting (Fig. 4.2B).

The lattice parameters a, b, and c are calculated by the (Eq. (4)).

(for cubic system, a=b=c)

$$\frac{1}{a^2} = \frac{1}{a^2}(h^2 + k^2 + l^2) \quad (4)$$

where h, k, and l are miller indices of the peak corresponding to the major refraction planes, d is the interplanar spacing of atomic planes, which was calculated by the Bragg equation (Eq. (5))

$$n\lambda = 2d\sin\theta \quad (5)$$

The lattice parameters obtained from the XRD data of the synthesized $Zn_{1-2x}Fe_xNi_xS$ NPs decrease in a range of 5.3664−5.2469Å with increasing the dopants content confirming the minimum distortion in the lattice structure in most of the cases. The doping of $Ni_{0.07}$ in ZnS distinctly decrease the lattice constant compared to $Ni_{0.05}$ and that of pristine ZnS which confirms the incorporation of all dopants in the host lattice as radii of Ni^{+2} is lesser than Zn^{+2}, While doping of $Fe_{0.07}$ results in an increase of lattice parameter in comparison to $Fe_{0.05}$ confirms the successful incorporation of dopant in the host lattice as ionic radii of Fe^{+2} (77pm) is larger than Zn^{+2}(74pm). Upon doping, the surface restructuring or the localized disturbances in the lattice results in micro strain, which could be seen in all the synthesized NPs (Table 4.2).

Further, energy dispersive spectra (EDS) were recorded at room temperature to confirm the amount of dopants in the host (Fig. 4.3A-G). EDS spectra reveal that all dopants are successfully incorporated in the synthesized ZnS.

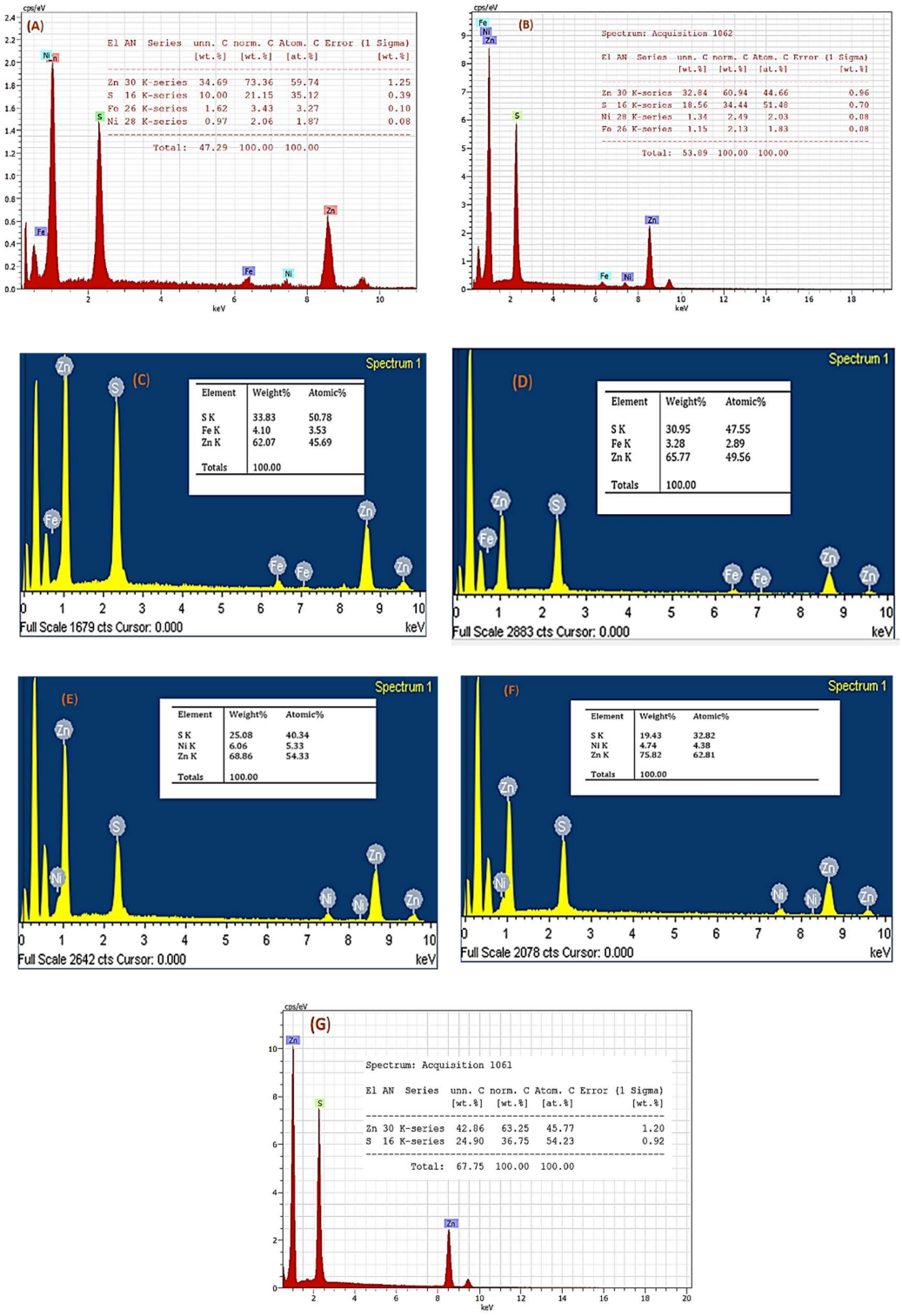

Fig. 4.3. EDX spectra of synthesized ZnS NPs (a) $Zn_{1-0.14}Fe_{0.07}Ni_{0.07}S$(b) $Zn_{1-0.10}Fe_{0.05}Ni_{0.05}S$ (c) $Zn_{1-0.07}Fe_{0.07}S$(d) $Zn_{1-0.05}Fe_{0.05}S$(e) $Zn_{1-0.07}Ni_{0.07}S$ (f) $Zn_{1-0.05}Ni_{0.05}S$ (G) pristine ZnS NPs.

Table 4.2 Parameters evaluated from PXRD and W-H plots.

	sample	Average crystallite Size by Scherrer's Formula (nm)	Effective crystallite Size by Williamson-Hall plot (nm)	Strain ($\times 10^{-3}$)	Lattice parameters (A°)
1.	$Zn_{1-0.14}Fe_{0.07}Ni_{0.07}S$	2.2	6.2	0.5416	5.2469
2.	$Zn_{1-0.10}Fe_{0.05}Ni_{0.05}S$	1.8	5.6	2.9058	5.2997
3.	$Zn_{1-0.07}Fe_{0.07}S$	1.9	4.5	0.309	5.3519
4.	$Zn_{1-0.05}Fe_{0.05}S$	3.0	6.1	0.2255	5.2469
5.	$Zn_{1-0.07}Ni_{0.07}S$	1.0	4.1	1.9899	5.2522
6.	$Zn_{1-0.05}Ni_{0.05}S$	1.6	2.1	1.9485	5.3555
7.	Pristine	2.8	5.5	0.1966	5.3664

The morphology and crystallographic study were carried out by using HRTEM analysis. HRTEM images show that the morphology of all the synthesized material is spherical. Selected Area Electron Diffraction (SAED) patterns show the amorphous nature of the synthesized NPs and corresponding planes can be indexed as shown in the figures. (Fig.4.4 a (A1-C3) and 4.4 b (D1-G3)).

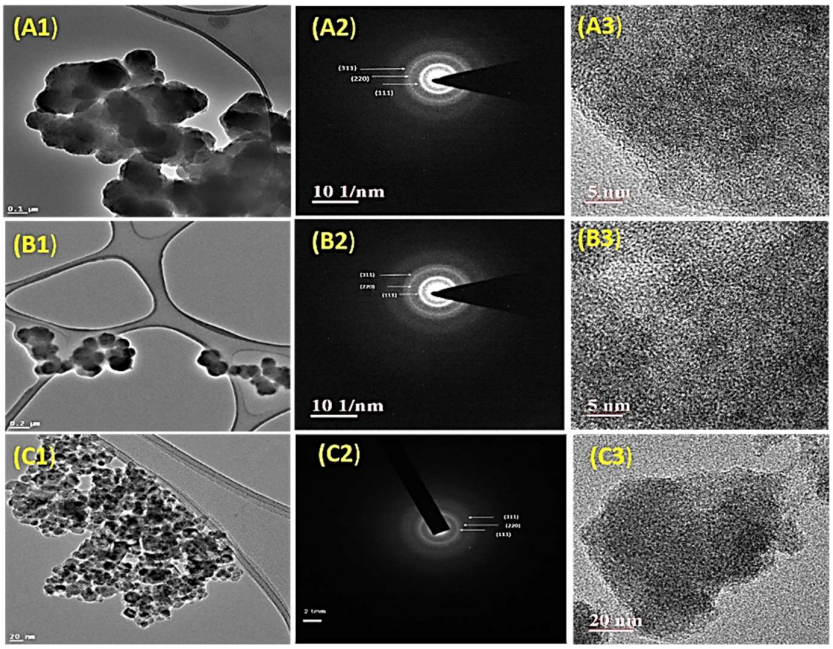

Fig.4.4a: HRTEM images, SAED patterns, and Lattice fringes of (A1), (A2), and (A3) ZnS with $Zn_{1-0.14}Fe_{0.07}Ni_{0.07}S$ (B1), (B2) and (B3) ZnS with $Zn_{1-0.10}Fe_{0.05}Ni_{0.05}S$ and (C1), (C2) and (C3) $Zn_{1-0.07}Fe_{0.07}S$.

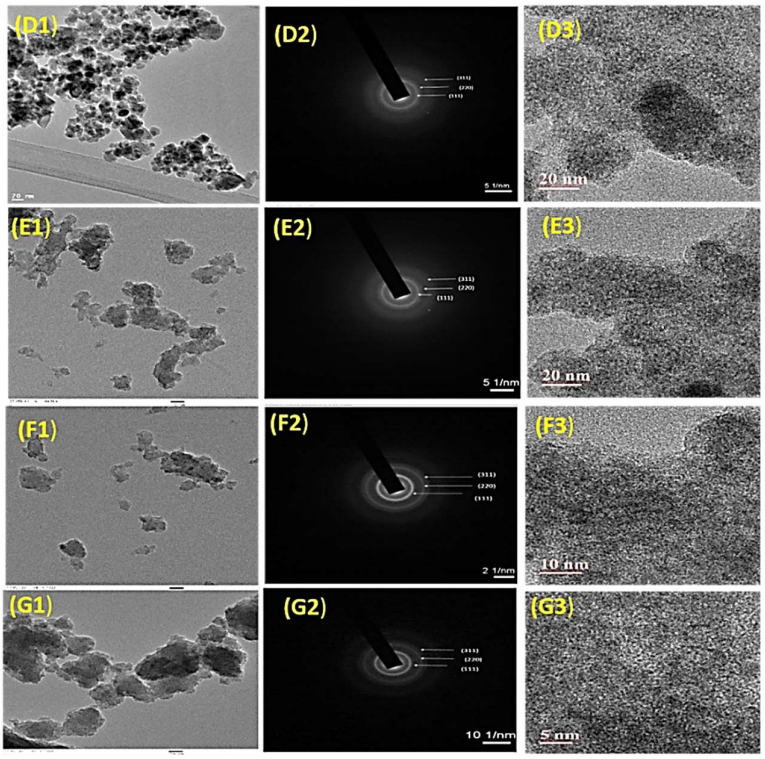

Fig.4.4 b: HRTEM images, SAED patterns and Lattice fringes of ZnS (D1), (D2) and (D3) for $Zn_{1-0.07}Fe_{0.07}S$ (E1), (E2) and (E3) for $Zn_{1-0.07}Ni_{0.07}$ S (F1), (F2) and (F3) $Zn_{1-0.05}Ni_{0.05}S$ (G1), (G2) and (G3) for pristine.

EDS mapping was also carried out to study the distribution of dopants in the host matrix, Fig. 4.5a (A-F), 4.5b (A-F), and 4.5c (A-D) display the energy-dispersive X-ray spectrometry mapping of the synthesized materials. SEM images indicate the spherical shapes of all the synthesized NPs.

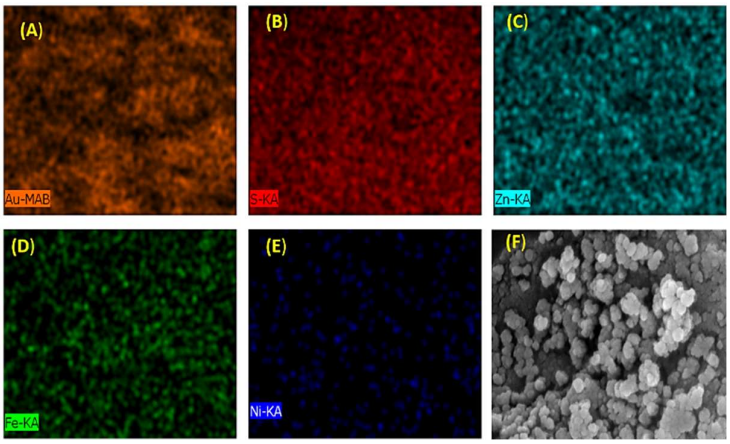

Fig. (4. 5a). SEM images (A and B) of as-synthesized co-doped $Zn_{1-0.14}Fe_{0.07}Ni_{0.07}S$ with elemental mapping as (C) S (red), (D) Zn (cyan), (E)Fe (green) and (F) Ni (blue).

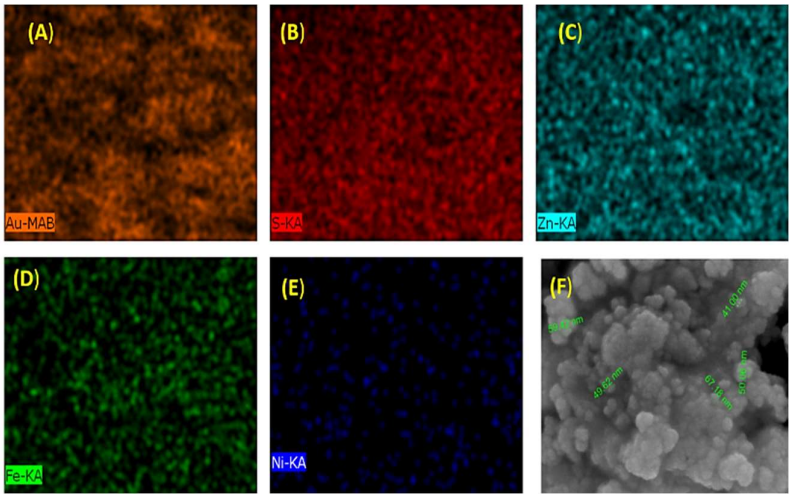

Fig. (4.5b). SEM images (A and B) of as-synthesized co-doped $Zn_{1-0.10}Fe_{0.05}Ni_{0.05}S$ with elemental mapping as (C) S (red), (D) Zn (cyan), (E)Fe (green), and (F) Ni (blue).

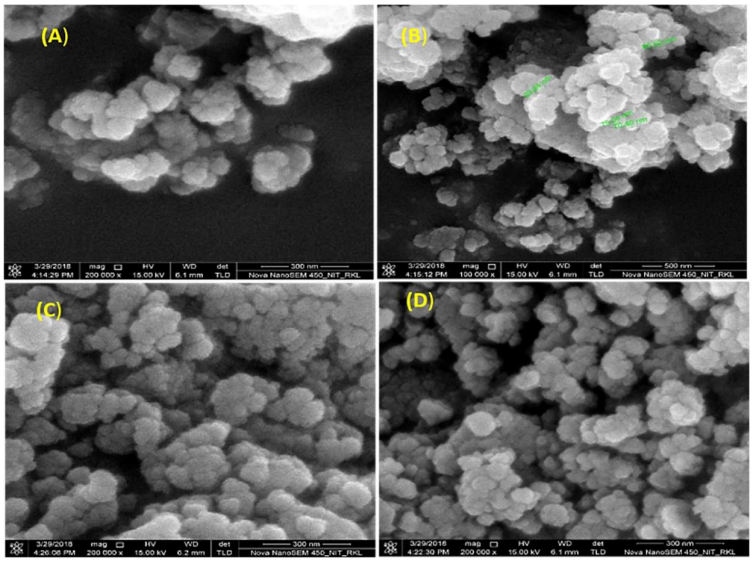

Fig. (4.5c). SEM images of (A) $Zn_{1-0.07}Fe_{0.07}S$ (B) $Zn_{1-0.05}Fe_{0.05}S$ (C) $Zn_{1-0.07}Ni_{0.07}S$ (D) $Zn_{1-0.05}Ni_{0.05}S$.

For the optical study of the as-synthesized NPs, UV- Vis absorption spectra were recorded in the range of 200-400 nm. The strongest excitonic absorption peak was observed in the range of 286- 295 nm (Fig. 4.6).

At nano regime, the optical properties become sensitive to the parameters like shape, size, agglomeration state, and refractive index near the nanoparticle surface etc. UV-Vis spectroscopy is an important tool for the characterization of the nanomaterials. In UV spectra

of the nano material, the absorption edge display a blue shift compared to the bulk ZnS due to the quantum confinement effect.[26]

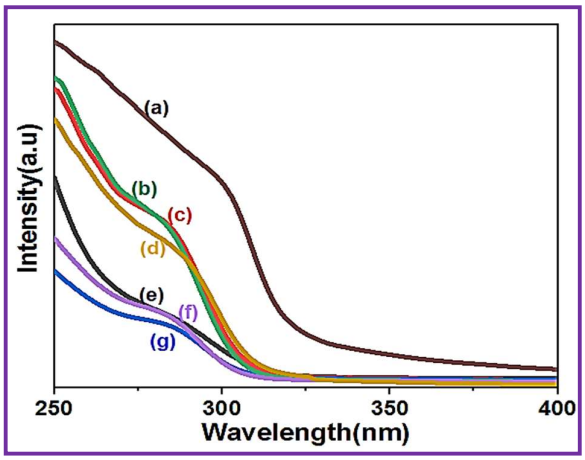

Fig. 4.6. Uv Spectra (A) and corresponding Fluorescence spectra (B) (a) $Zn_{1-0.14}Fe_{0.07}Ni_{0.07}$ (b) $Zn_{1-0.10}Fe_{0.05}Ni_{0.05}S$ (c) $Zn_{1-0.07}Fe_{0.07}S$ (d) $Zn_{1-0.05}Fe_{0.05}S$ (e) $Zn_{1-0.07}Ni_{0.07}S$ (f) $Zn_{1-0.05}Ni_{0.05}S$ (g) pristine ZnS NPs.

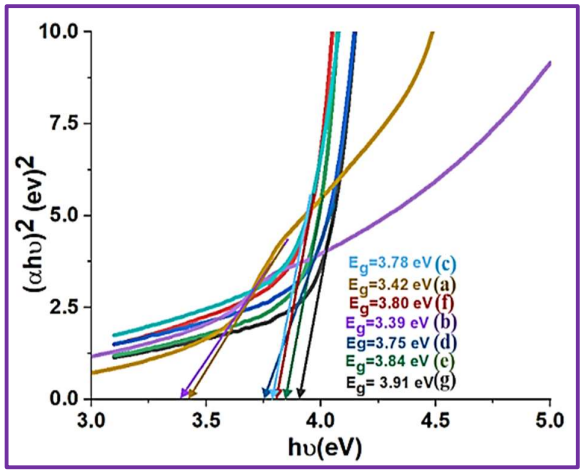

Fig. 4.7. $(\alpha h\nu)^2$v/s hν plots of ZnS NPs having (a) $Fe_{0.07}$ $Ni_{0.07}$ (b) $Fe_{0.05}$ $Ni_{0.05}$ (c) $Fe_{0.07}$ (d) $Fe_{0.05}$ (e) $Ni_{0.07}$ (f) $Ni_{0.05}$ and (g) Pristine ZnS nanoparticles.

The optical direct band-gap was determined from the tauc relationship by extrapolating the straight-line to the hν-axis [Eq. (6)][27]

$$(\alpha h\nu)^2 = B(h\nu - E_g) \qquad (6)$$

where, $(h\nu)$ is the photon energy, and, the absorption coefficients ($\alpha = 4\pi\kappa/\lambda$, κ absorption, and λ is the wavelength in nm), and α is a constant.

The calculated energy band gaps are reported in (Fig. 4.7 a-g, and Table 4.3).

On comparing the band-gaps of the bulk and co-doped as-synthesized ZnS NPs, it can be observed that the band-gap increases with increasing the dopants' amount. This is due to the discreteness of the bands on decreasing the particle size.

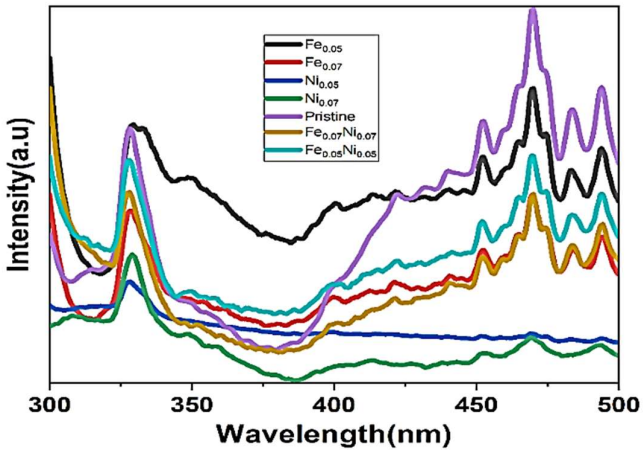

Fig. 4.8 Fluorescence spectra of ZnS Nanoparticles.

Fig. 4. 8 shows room temperature PL spectra of synthesized nanoparticles capped by 2-ME under 297 nm excitation. The emission at 410 nm is attributed to the charge carrier recombination from V_s to VB, whereas the peak at 460 nm is due to the transfer of electron from V_s to V_{Zn}. The emission at 490 nm indicates the presence of excess Zn ions on the surface.[28]

The surface charge of all the synthesized NPs were studied by Zeta Potential (ζ) measurement (Table 4.3), the values of surface charge suggest good stability of all the synthesized nanoparticles in a colloidal solution.

Table 4.3 Absorption edge, Bandgap, the surface charge of synthesized ZnS NPs.

S. No	ZnS NPs	Absorption maxima	Band gap (eV)	D_{DLS} (nm)	Zeta Potential (mV)
1.	Bulk	337	3.66	-	
2.	Pristine	312	3.95	65.9	-30.55
3.	$Zn_{1-0.14}Fe_{0.07}Ni_{0.07}S$	325	3.49	140.5	-23.64
5.	$Zn_{1-0.10}Fe_{0.05}Ni_{0.05}S$	305	3.41	120.5	-25.87
6.	$Zn_{1-0.07}Fe_{0.07}S$	310	4.0	159.4	-37.56
7.	$Zn_{1-0.05}Fe_{0.05}S$	313	4.05	141.4	-45.95
8.	$Zn_{1-0.07}Ni_{0.07}S$	317	4.01	23.3	-41.77
9	$Zn_{1-0.05}Ni_{0.05}S$	308	4.02	26.9	-16.99

The FTIR spectra of ME capped Zns NPs were recorded in the range of 4000-500 cm^{-1}at RT (Fig: 4.9A (a-g), and 4.9B (enlarged region)). Spectral bands occurring at 480 cm^{-1} and 653 cm^{-1} represented the stretching vibrations of Zn-S. The peak at 1000 cm^{-1} suggests the presence of resonance between vibrational modes of sulfide ions in the ZnS crystal structure.[29] The bands at 1061 and 1416 $cm^{-1}$are characterized by the C-O stretching and -CH_2- bending respectively. The peaks at 1631 and 2840 cm^{-1} are due to the microstructure formation.[29,30] The broad absorption peaks in the range of 3290–3498 cm^{-1} correspond to the –OH group indicates the surface adsorbed water during the synthesis of the material.

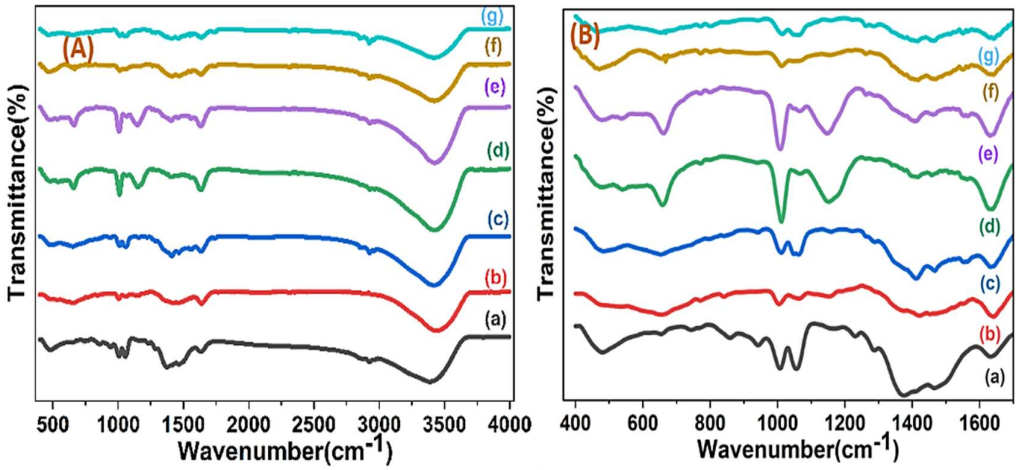

Fig. 4.9 (A) IR spectra and (B) enlarge region (350cm^{-1} to 1700cm^{-1}) of synthesized ZnS Nps (a) Pristine (b) $Zn_{1-0.14}Fe_{0.07}Ni_{0.07}S$ (c) $Zn_{1-0.10}Fe_{0.05}Ni_{0.05}S$ (d) $Zn_{1-0.07}Fe_{0.07}S$ (e) $Zn_{1-0.05}Fe_{0.05}S$ (f) $Zn_{1-0.07}Ni_{0.07}S$ (g) $Zn_{1-0.05}Ni_{0.05}S$.

A room temperature VSM study was carried out to investigate the magnetic behavior of the as-synthesized NPs as a function of the applied magnetic field of -15000 to +15000 Oe. The saturation magnetization increases with the increase in concentration of the dopants in the case of mono-doped NPs (Table 4.4), while in the case of a co-doped system saturation magnetization decreases with the increase in the concentration of both dopants (Fig.4.10A (a-b), 4.10B (c-f)). At room temperature the highest ferromagnetism was observed for $Zn_{1-(Fe0.05+Ni0.05)}S$ while super paramagnetism was observed for $Zn_{1-0.14}Fe_{0.07}Ni_{0.07}S$. The enhanced ferromagnetism in $Zn_{1-0.10}Fe_{0.05}Ni_{0.05}S$ may be attributed to the intrinsic coupling between the doped Fe and Ni atoms (synergic effect) and not due to the individual cluster Fe and Ni atoms in the ZnS lattice, as no other phases have been seen in XRD analysis.

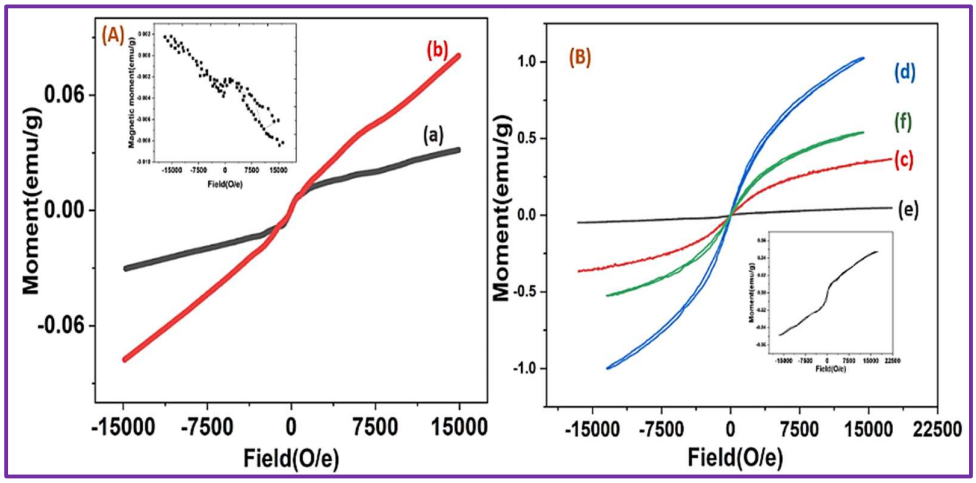

Fig. 4.10 (A)VSM (a) $Zn_{1-0.14}Fe_{0.07}Ni_{0.07}S$ (b) $Zn_{1-0.10}Fe_{0.05}Ni_{0.05}S$ (inset pristine ZnS) and 4.10(B) (c) $Zn_{1-0.07}Fe_{0.07}S$ (d) $Zn_{1-0.10}Fe_{0.05}S$ (e) $Zn_{1-0.07}Ni_{0.07}S$ (f) $Zn_{1-0.05}Ni_{0.05}S$.

Table 4.4 The VSM data of ZnS Co-doped/mono-doped NPs at room temperature with different amounts of dopants. (Maximum field 15000 Oe).

Sample	Susceptibility χ	Retentivity Mr(emu/g) 10^{-3}	Saturation Ms(emu/g) 10^{-3}	Coercivity H_c (Oe)
Pristine	-0.097	2.29	19.25	320.83
$Zn_{1-0.14}Fe_{0.07}Ni_{0.07}S$	0.010344E-3	1.33	37.94	4.91
$Zn_{1-0.10}Fe_{0.05}Ni_{0.05}S$	0.02224E-3	1.26	81.57	172.81
$Zn_{1-0.07}Fe_{0.07}S$	0.10034E-3	3.39	0.36	4.40
$Zn_{1-0.10}Fe_{0.05}S$	0.2753E-3	11.84	1.01	56.36
$Zn_{1-0.07}Ni_{0.07}S$	0.0144E-3	2.80	52.924	9.67
$Zn_{1-0.05}Ni_{0.05}S$	0.006721	1.33	24.658	46.21

The electrochemical analyses were carried out to understand the effect of dopant ions on the redox behaviour of the material. The CV curves (Fig. 4.11A (a-b) and 4.11B (c-f)) show the anodic current at negative potential. On introduction of Ni^{2+} and $Fe^{+2,}$ the additional irreversible peak appears during the oxidation scan at -0.70V for $Zn_{1-0.05}Ni_{0.05}S$, -0.73V for $Zn_{1-0.07}Ni_{0.07}S$ while -0.73V for $Zn_{1-0.05}Fe_{0.05}S$ and -0.74V for $Zn_{1-0.07}Fe_{0.07}S$ corresponds to the standard oxidation potential for Ni^{2+}/Ni^{3+} and Fe^{+2}/Fe^{+3} vs NHE respectively. Similar additional peaks were also observed in co-doped as-synthesized systems and their current

intensity increases with increasing dopant ion concentration. Redox behaviour was observed in the case of $Zn_{1-0.14}Fe_{0.07}Ni_{0.07}S$ while in $Zn_{1-0.10}Fe_{0.05}Ni_{0.05}S$ only oxidation behavior can be seen. Electrochemical impedance spectral (EIS) measurements (Fig. 4.11C) were performed to study the conducting behavior of the material. From the impedance spectra, it can be observed that $Fe_{0.07}$ has the highest conductivity. Mott–Schottky (MS) (Fig. 4.11D, Table 4.5, 4.6) measurements were carried out to trace the origin and fate of charge carriers in the material. The positive slope indicates the n-type semiconductor nature of all the synthesized samples, the highest donor density was observed in $Zn_{1-0.10}Fe_{0.05}Ni_{0.05}S$. This requires less potential bias to achieve the Fermi level from the depletion region.

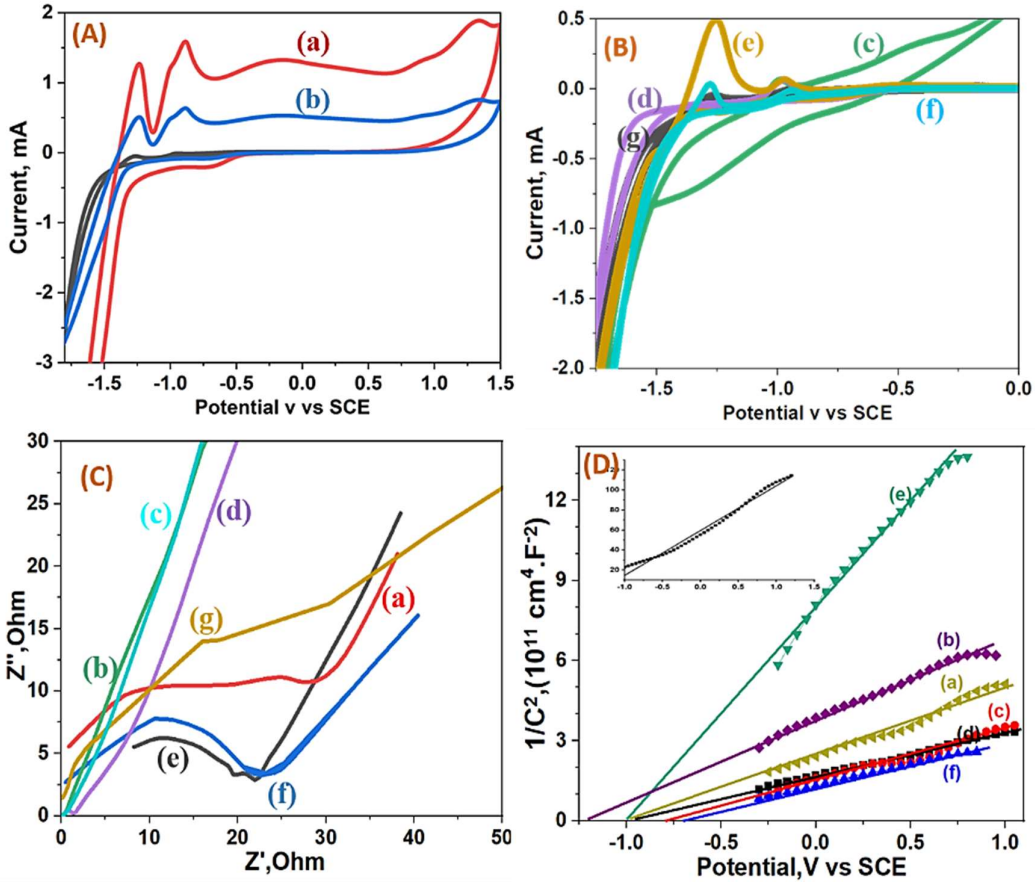

Fig.4.11. (A) Cyclic voltammogram of as-synthesized ZnS NPs as a working electrode in an aqueous solution, (a) $Zn_{1-0.14}Fe_{0.07}Ni_{0.07}S$ (b) $Zn_{1-0.10}Fe_{0.05}Ni_{0.05}S$(c) $Zn_{1-0.07}Fe_{0.07}S$ (d) $Zn_{1-0.05}Fe_{0.05}S$ (e) $Zn_{1-0.07}Ni_{0.07}S$ (f) $Zn_{1-0.05}Ni_{0.05}S$ (C) EIS Nyquist plots (D) Normalized Mott–Schottky plot (inset; pristine ZnS). (Scan rate: 25 mV/Sec. RE = saturated calomel electrode (SCE), CE = platinum wire).

Flat-band potentials were calculated by extrapolating the straight line to X-axis ($1/C^2 = 0$) (Fig. 4.12).[23]

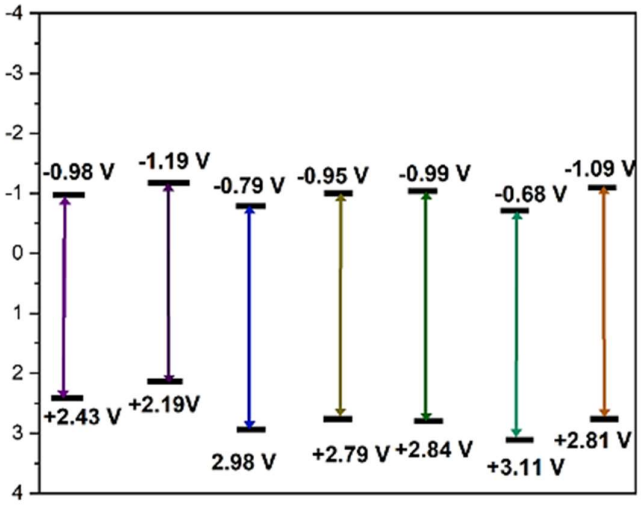

Fig.4.12 Flat band potential.

Table 4.5 MS and EIS data of pristine and Fe doped ZnS NPs.

Samples	Conductivity (10^6S/cm)	Donor density (N_d)10^{20}/cm^{-3}
0	3.70	0.03
$Zn_{1-0.10}Fe_{0.05}Ni_{0.05}S$	34.74	4.66
$Zn_{1-0.14}Fe_{0.07}Ni_{0.07}S$	49.02	0.68
$Zn_{1-0.07}Fe_{0.07}S$	203.00	1.04
$Zn_{1-0.05}Fe_{0.05}S$	189.00	0.88
$Zn_{1-0.07}Ni_{0.07}S$	35.56	1.02
$Zn_{1-0.05}Ni_{0.05}S$	45.24	0.21

Table5. Electronic band structure of the photocatalyst.

Samples	The slope from the MS plot (10^{11})	E_{cb}~ E_{fb} vs. SCE V	E_{cb}~ E_{fb} vs. NHE V	Bandgap energy eV	E_{VB} V
0	44.88	-1.0901	-0.8486	3.91	+2.81
$Zn_{1-0.14}Fe_{0.07}$ $Ni_{0.07}S$	2.41	-0.9821	-0.7406	3.42	+2.43
$Zn_{1-0.10}Fe_{0.05}$ $Ni_{0.05}S$	3.03	-1.1948	-0.9533	3.39	+2.19
$Zn_{1-0.07}Fe_{0.07}S$	1.87	-0.7972	-0.5557	3.78	+2.98
$Zn_{1-0.05}Fe_{0.05}S$	1.62	-0.9542	-0.7127	3.75	+2.79
$Zn_{1-0.07}Ni_{0.07}S$	7.79	-0.9976	-0.7561	3.84	+2.84
$Zn_{1-0.05}Ni_{0.05}S$	1.60	-0.6890	-0.4475	3.80	+3.11

$E_{NHE} = E_{SCE} + 0.2415$

To know the surface area of the as-synthesized NPs, BET-specific surface area (SBET) was determined by nitrogen adsorption-desorption isotherms (Fig. 4.13 A-G). The parameters obtained are given in Table 4.7.

Table 4.7 BET parameters.

Parameters	Pristine	$Zn_{1-0.14}Fe_{0.07}Ni_{0.07}S$	$Zn_{1-0.10}Fe_{0.05}Ni_{0.05}S$	$Zn_{1-0.07}Fe_{0.07}S$	$Zn_{1-0.05}Fe_{0.05}S$	$Zn_{1-0.07}Ni_{0.07}S$	$Zn_{1-0.10}Ni_{0.05}S$
SBET(m^2/g)	98.03	73.40	108.15	136.12	149.52	152.49	5.32
Average pore diameter(A°)	94.36	103.02	37.85	44.00	42.25	62.96	108.69
Pore volume(cm^3/g)	0.00	0.00	0.01	0.023	0.00	0.024	0.00
Total volume in pores(cm^3/g)	0.16	0.06	0.07	0.11	0.10	0.12	0.00
Total area in pores(m^2/g)	53.91	45.63	39.03	39.21	74.20	50.98	2.50

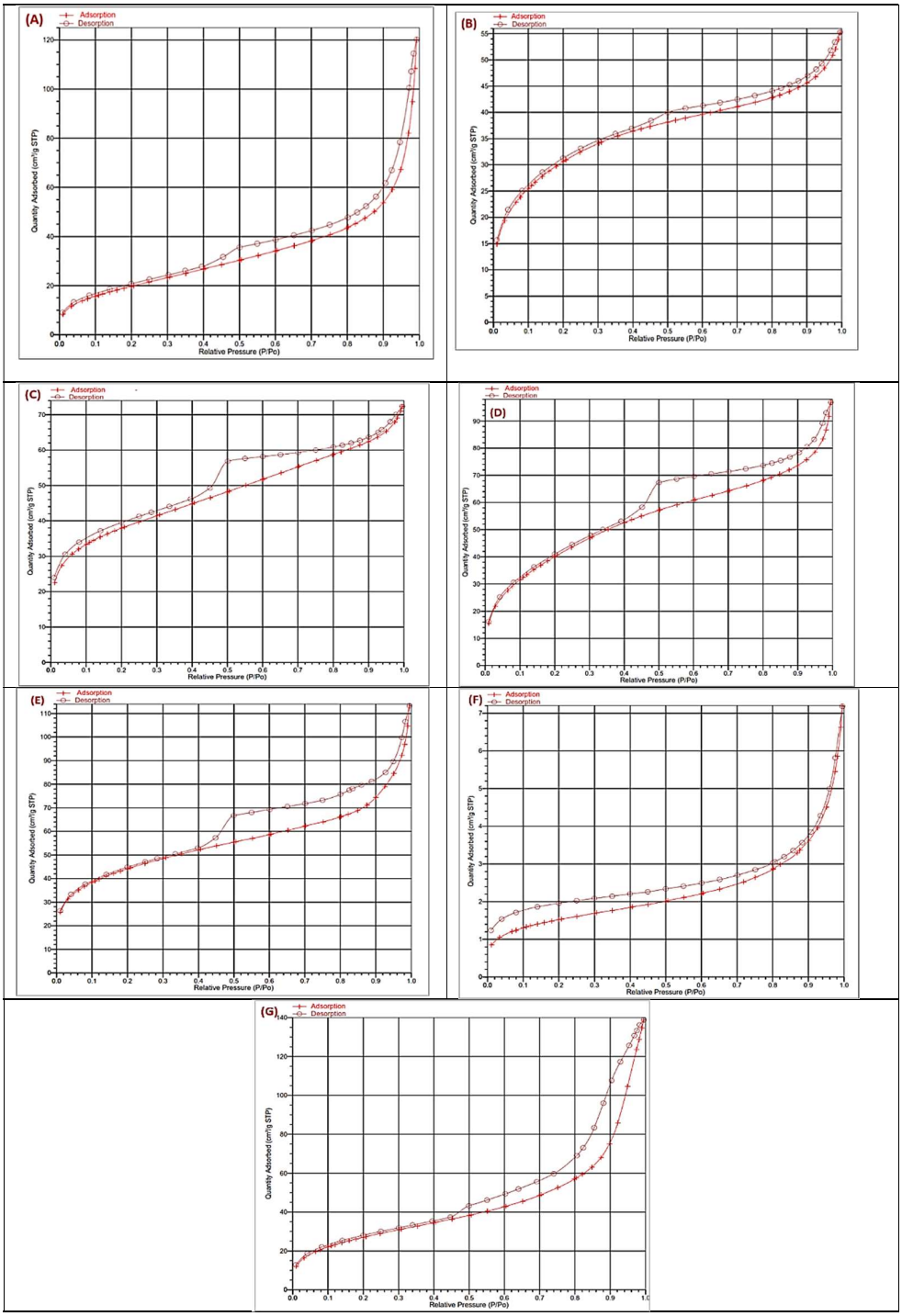

Fig. 4.13. Nitrogen adsorption-desorption isotherms for synthesized ZnS NPs (A) $Zn_{1-0.14}Fe_{0.07}Ni_{0.07}S$ (B) $Zn_{1-0.10}Fe_{0.05}Ni_{0.05}S$ (C) $Zn_{1-0.07}Fe_{0.07}S$ (D) $Zn_{1-0.05}Fe_{0.05}S$ (E) $Zn_{1-0.07}Ni_{0.07}S$ (F) $Zn_{1-0.05}Ni_{0.05}S$ (G) Pristine.

Evaluation of photocatalytic activity

The photocatalytic performance of as-synthesized ZnS NPs.

The time-dependent photocatalytic activities of as-synthesized NPs are shown in (Fig.4.14). Photocatalytic activity was also evaluated spectrophotometrically with respect to change in the absorption intensity (λ_{max} at 546nm) of aqueous solution of RhB. The % decolorization efficiency of the material was calculated as Eq.8

$$\% \text{ Efficiency} = 100\times \frac{[A_o - A]}{A_o} = 100\times \frac{[C_o - C]}{C_o} \quad (8)$$

Where, A_o, A, C_o, and C are initial absorbance, absorbance after irradiation at various time intervals, initial concentration of the solution, and concentration of dye after irradiation at various time intervals, respectively.

The plot of ln C_o/C_t vs irradiation time is a straight line and passes through the origin Fig. 4.15A indicates the first-order decay kinetics. Maximum rate can be achieved in presence of $Zn_{1-0.10}Fe_{0.05}Ni_{0.05}S$. the PL spectra of illuminated basic solution of terephthalic acid in presence of $Zn_{1-0.10}Fe_{0.05}Ni_{0.05}S$ doped ZnS NPs at different time intervals were recorded Fig. 4.15B under high pressure mercury vapour (HPMV) lamp and corresponding time vs c_t/c_o graph were plotted Fig. 4.15C and The values of the rate constant for all the synthesized ZnS samples are given in Table 4.7.

As per literature, Fe-doped ZnS and Ni-doped ZnS NPs revealed their ability to degrade RhB in an aqueous medium. However, when Fe and Ni ions are co-doped into the ZnS matrix at a 5% level, the photocatalytic efficiency is enhanced. 5% (Fe/Ni) co-doped ZnS NPS are the most capable for completely removal of dye from the solution within 5.33 h (Fig. 4.14B and Fig.4.16). Hence, it can be concluded from the results that on introduction of Fe with co-doping of Ni in the ZnS lattice host matrix can synergistically enhance the photocatalytic activity. Further, the photocatalytic efficiency decreased on increasing the dopants concentration from 5% to 7%. So, it can be concluded that the wurtzite phase is not always responsible for the enhanced photocatalytic efficiency. Calculated rate constant and degradation efficiency are reported in (Table 4.7).

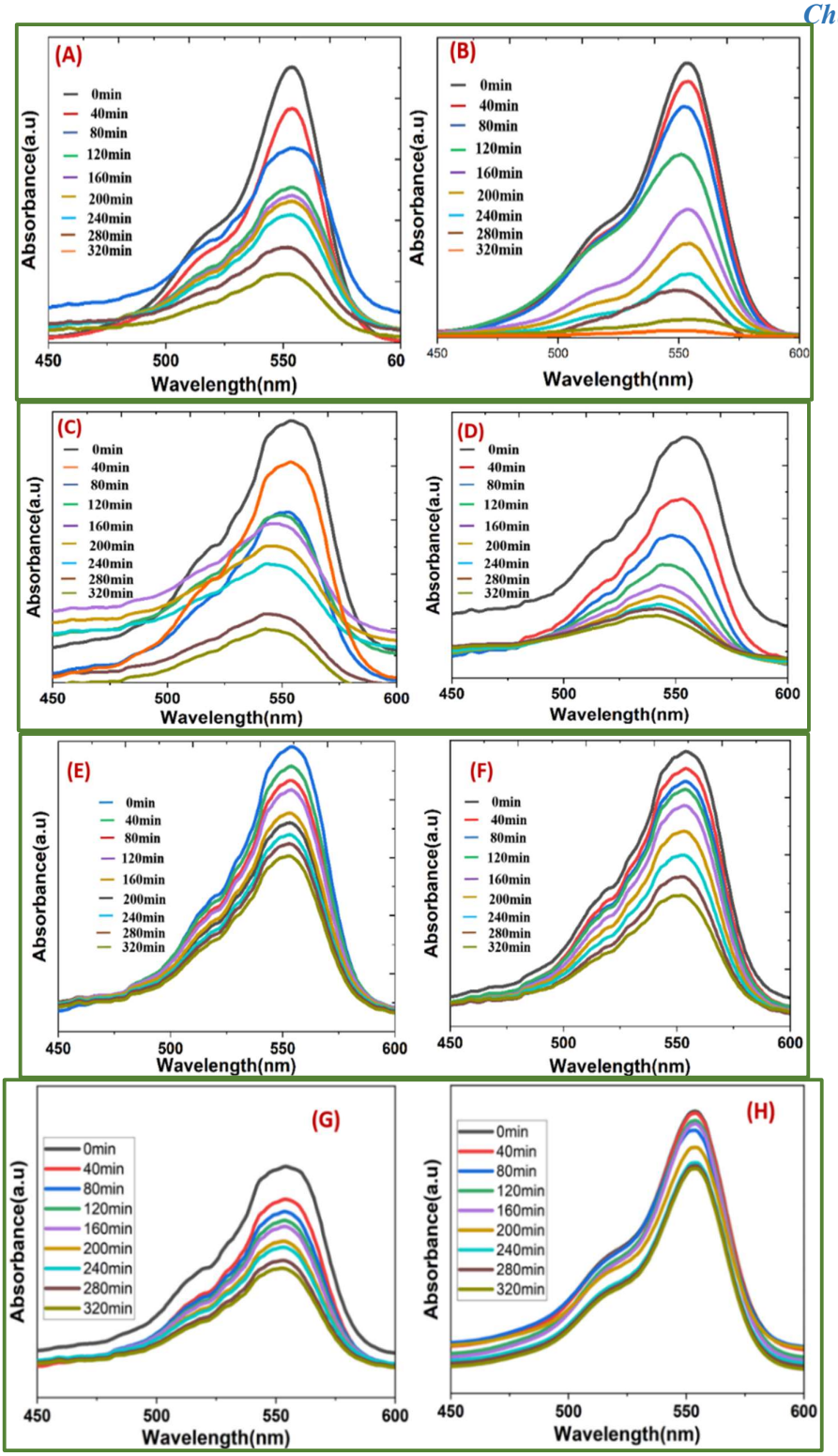

Fig. 4.14 Photocatalytic degradation of RhB dye in terms of diminishing intensity of λ max at 554nm in presence of (A) $Zn_{1-0.14}Fe_{0.07}Ni_{0.07}S$ (b) $Zn_{1-0.10}Fe_{0.05}Ni_{0.05}S$ (C) $Zn_{1-0.07}Fe_{0.07}S$ (D) $Zn_{1-0.05}Fe_{0.05}S$ (E) $Zn_{1-0.07}Ni_{0.07}S$ (F) $Zn_{1-0.05}Ni_{0.05}S$ (G) Pristine ZnS (H) Bulk ZnS.

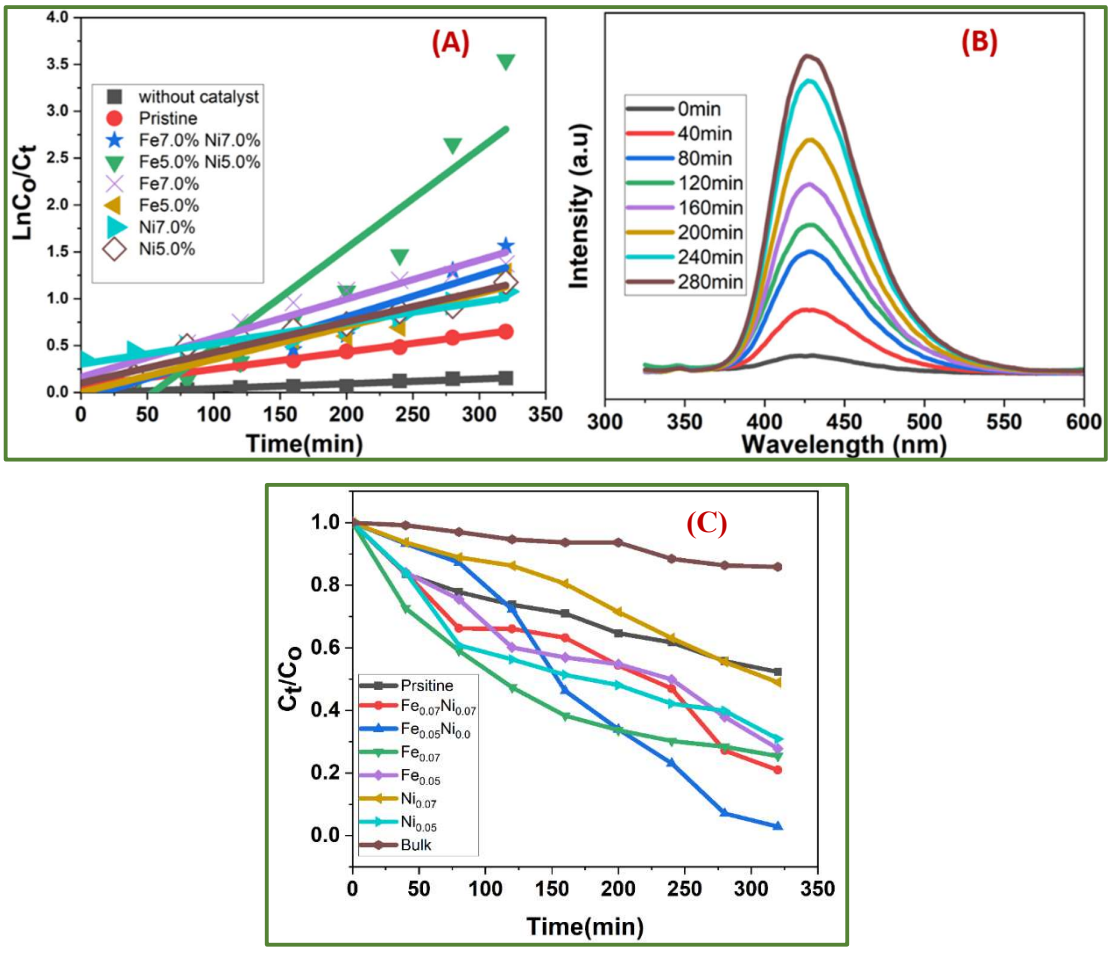

Fig.4.15 (A) Ln Co/C_t VS Time (B) PL intensity of basic solution of terephthalic acid under HPMV irradiation at different time intervals in presence of $Zn_{1-0.10}Fe_{0.05}Ni_{0.05}S$ NPs. (c) Photodegradation of RhB under HPMV irradiation.

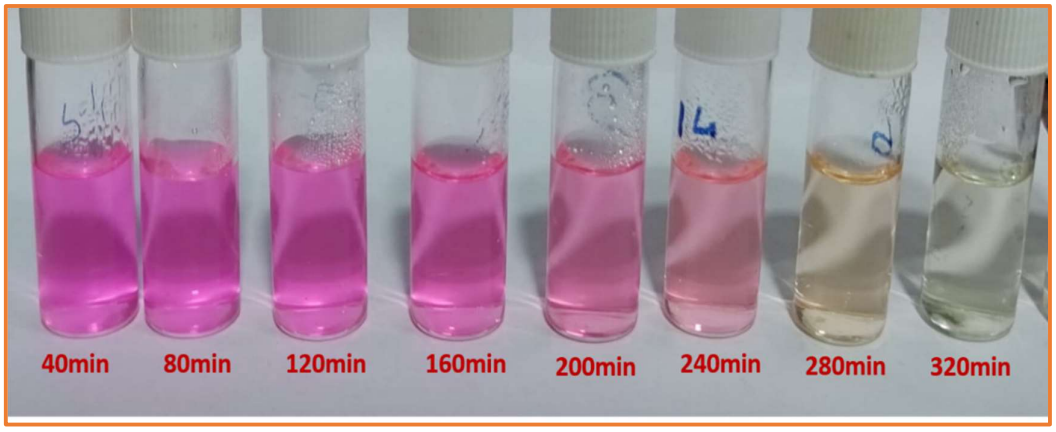

Fig. 4.16 Photographs showing the change in color with a given interval for photocatalytic RhB dye removal in presence of $Zn_{1-0.10}Fe_{0.05}Ni_{0.05}S$

Table 4.8 Degradation of an aqueous solution of RhB dye under white light irradiation after 320 min.

Samples	% Degradation	Rate constant (h^{-1})	correlation coefficient (R^2)
Pristine Zns	47.69	0.1906	0.972
$Zn_{1-0.14}Fe_{0.07}$ $Ni_{0.07}S$	79.06	0.2934	0.943
$Zn_{1-0.10}Fe_{0.05}$ $Ni_{0.05}S$	97.12	0.6655	0.934
$Zn_{1-0.07}Fe_{0.07}S$	74.60	0.2571	0.953
$Zn_{1-0.05}Fe_{0.05}S$	72.23	0.1818	0.943
$Zn_{1-0.07}Ni_{0.07}S$	65.87	0.2017	0.967
$Zn_{1-0.05}Ni_{0.05}S$	69.13	0.2220	0.984
Without any catalyst	14.13	0.0285	0.956

DFT Study

Theoretical Models and Computational Details

The first principle study by Rodriguez et al[31] on Ni-doped ZnS shows the influence of Ni in low energy transition and increased optical absorbance. While the effect of varying the Fe doping, in turn, tuning the band-gap by this way, on the optoelectronic and fluorescence property of ZnS NPs was studied very well by ab-initio techniques.[32] An intensive work by Wan et al. [33] on visible-light photocatalysis through a metal/non-metal codoping display the significance of V/Cu, and N/ F pair combination resulting in an enhancement of variety of physical properties with lower recombination rate. Cu-F [33] co-doping being relevant among the others. While the importance of p_π-d_π conjugation in Mn+Ni [34], Ho+Ag [35], and Al(Ga, In)+N [36] along with low resistivity were demonstrated. Despite its usability and abundance for overall electronic, optical, and magnetic applications, photoactivity study is limited and needs special attention considering the energy crisis. We have performed a computational study for the electronic, optical, magnetic, and photocatalytic properties of the above as-synthesized materials and based on the computational results the amount of dopant and co-dopants was varied to achieve the optimum performance.

Theoretical Models

ZnS-ZB and ZnS-WZ phases are performed while ZnS-ZB is found more stable than ZnS-WZ. ZnS-ZB is a cubic structure with a=b=c=5.409 Å.[33] We considered 2 X 2 X 1 supercell (32

atoms) by extending a and b basis vector directions. Mono-doping of Fe and Ni by substituting Zn atom ($Zn_{Fe}S$, $Zn_{Ni}S$), 6.125% doping similar to experimental study, while for co-doping two configuration i. interacting Fe, Ni ($Zn_{Fe,Ni}S_{Int}$) attached by common S atom and ii. Non-interacting ($Zn_{Fe,Ni}S_{Non\text{-}Int}$) TM impurity is considered as shown in Fig.4.17 Separate configuration consideration to study S-TM p_{π}-d_{π} conjugation and stability by total energy calculations is the pre-requisite criterion.

Spin-polarized density functional theory calculations were performed using the pseudopotential method by solving Kohn-Sham[37,38] equations for energy calculations embodied in QUANTUM ESPRESSO [39]code. Perdew-Burke-Ernzerof (PBE)[40] functional following generalized gradient approximation is used to include the exchange-correlation interactions with ultrasoft pseudopotential. Wavefunction and charge density cutoff energy were converged and set to 60 and 540 Ry respectively, while a 6 X 6 X 6 k mesh grid was considered for achieving a threshold of 10^{-6} eV/atom in the SCF cycle. The unit cell of pristine-ZnS is undertaken volume convergence to reach the most stable lattice parameter as shown in Fig. 4.18. thereafter band structure, the density of states, absorption coefficient, and the magnetic moment was calculated.

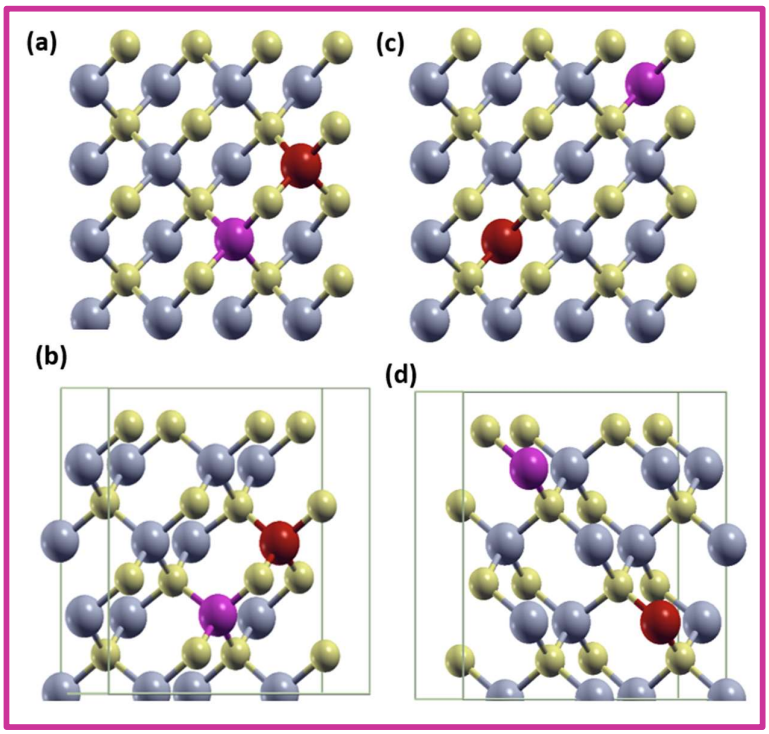

Fig. 4.17 Structure of (a, b) $Zn_{Fe,Ni}S_{Int}$ and (c, d) $Zn_{Fe,Ni}S_{Non\text{-}Int}$ geometry with side and tilted glance.

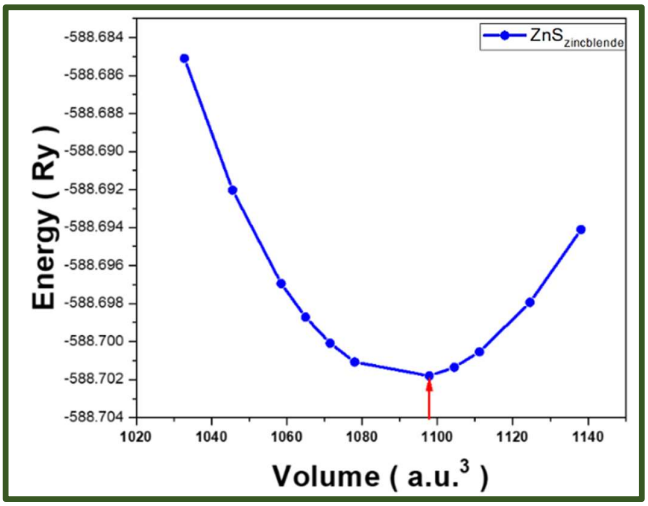

Fig. 4.18. Structural convergence test for pristine zinc sulfide in zinc blende phase.

Structural Properties

Structural optimization to achieve the most stable structure and accurate energy-based properties was done for all structures after the equilibrium lattice constant for pristine ZnS was adopted by volume convergence. a=b=c= 5.448 Å is computed and found in agreement with the experimental value of 5.41 Å[41] and henceforth used for electronic, optical, and magnetic property investigations. Lattice parameter and bond length variation on doping and co-doping is shown in Table. 1, due to the larger electronegativity of Fe, Ni the doping geometry showed a decrement in TM-S bond length along with the lattice parameter. While reduction of lattice parameter by 0.9% and 0.78% in x, y direction for $Zn_{Fe,Ni}S_{Int}$ and $Zn_{Fe,Ni}S_{Non\text{-}Int}$ results from the synergistic effect of substituted cationic radius and its electronegativity. The Fe-S bonding variation in interacting and non-interacting co-doped ZnS is attributed to the larger electronegativity of Ni hence leading to the formation of a charge transfer channel between substitutional cationic impurities. (Which will be discussed in a later section)

Theoretical thermodynamical stability of pristine and supercell geometry is a prerequisite to presenting the feasible reaction type system will achieve. To check the relative stability, defect formation energy (E_{form}) is computed as follows:

$$E_{form} = E_{System} - E_{Pristine} - \sum n_A \mu_A + \sum n_B \mu_B$$

Table 4.8 Calculated lattice parameters, bandgap, and magnetic moments of Fe and Ni-doped and co-doped ZnS (zinc blende) samples.

Sample	Lattice Parameters (Å)	E_{form} (meV/f. u.)	E^g (eV)	Magnetic Moment (μ_B/f.u.)	E_F (eV)	M-S (Å)	E_c (V)	E_v (V)	β
ZnS	a = b = c = 5.448	-	2.01	0.00	6.27	2.36	-0.18	1.83	0.07
$Zn_{Fe}S$	a = b = 10.849 c = 5.425	4.06	2.36	0.211	6.97	2.23	-0.37	1.99	0.11
$Zn_{Ni}S$	a = b = 10.857 c = 5.428	8.06	2.08	0.104	6.14	2.27	-0.22	1.86	0.13
$Zn_{Fe,Ni}S_{Int}$	a = b = 10.797 c = 5.399	12.37	2.57	0.305	6.80	2.21_{Fe} 2.10_{Ni}	-0.48	2.09	0.17
$Zn_{Fe,Ni}S_{Non-Int}$	a = b = 10.811 c = 5.4053	12.25	2.61	0.313	6.67	2.19_{Fe} 2.26_{Ni}	-0.50	2.11	0.10

Here, the total energy of ZnS ($E_{pristine}$), n_A, μ_A, and n_B, μ_B is the total number and chemical potential of host and substituent atoms in the system. The value of k_BT is 26 meV at room temperature and by our DFT calculation, we have a lower E_{form} predicting its successful synthesis and stability at room temperature. We show E_{form} in Table. 1, despite the large difference in Fe, Zn atomic radii $Zn_{Fe}S$ have the least E_{form} among others while $Zn_{Fe,Ni}S_{Non-Int}$ have lower endothermic energy requirements than $Zn_{Fe,Ni}S_{Non-Int}$. The same trend is seen in the lattice parameter and M-S bond length for the mono-doped system, with higher change and lower stability. The reason for this quest is in the charge transfer number between S-atom neighboring TM, the high electronegativity of the S atom is steering the stability criterion and is responsive to variation in the structural property. S atom acts as an efficient bridge forming a charge transfer channel between TM activating the whole surface. For $Zn_{Fe}S$, $Zn_{Ni}S$, $Zn_{Fe,Ni}S_{Int}$ and $Zn_{Fe,Ni}S_{Non-Int}$ $0.21e^-$, $0.13e^-$, $0.25e^-$(Fe)-$0.1e^-$(Ni) and $0.26e^-$(Fe)-$0.12e^-$(Ni) decrement in S atom from pristine S-ZnS is seen showing a direct relationship with structural stability. Meanwhile drastic Fe-S-Ni bond length decrement in $Zn_{Fe,Ni}S_{Int}$ is another reason for unstable equilibrium.

Electronic Properties

Extensive investigation of the ground state electronic property is shown by band structure, the density of states (DOS), spin-polarized DOS, and its respective projected DOS (PDOS) where the majority, minority charge carriers are shown on top and bottom. Fermi energy (E_F) for every system is shifted to zero energy for a better understanding of conduction (CB), valence

(VB), and intermediate bands (IB) while band gap (E_g) values have been tabulated and shown in the band structure. As shown in Fig.4.19, the band structure and DOS is aligned sidewise showing direct E_g at the gamma point on momentum space, the underestimation of E_g is a result of exchange-functional (PBE). Although our theoretical support is for an explanation of the relative position of states along with the rate of recombination and its role in high experimental photocatalytic efficiency thus it's widely accepted and elaborate.

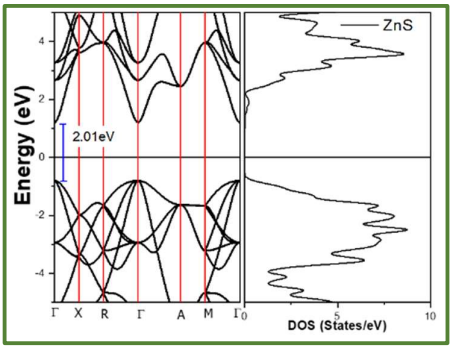

Fig. 4.19 Aligned band structure and density of states for zinc sulfide.

Increment of E_g relative to pristine along with the formation of IB is seen in Fe, Ni -mono, co-doped ZnS system as seen from Fig. 4.20 (a-d), Fig.4.21 TM-3d orbital contribute in the intermediate state and governs dispersion of band also seen from Fig. 4.22 (a-e, a_1-e_1).

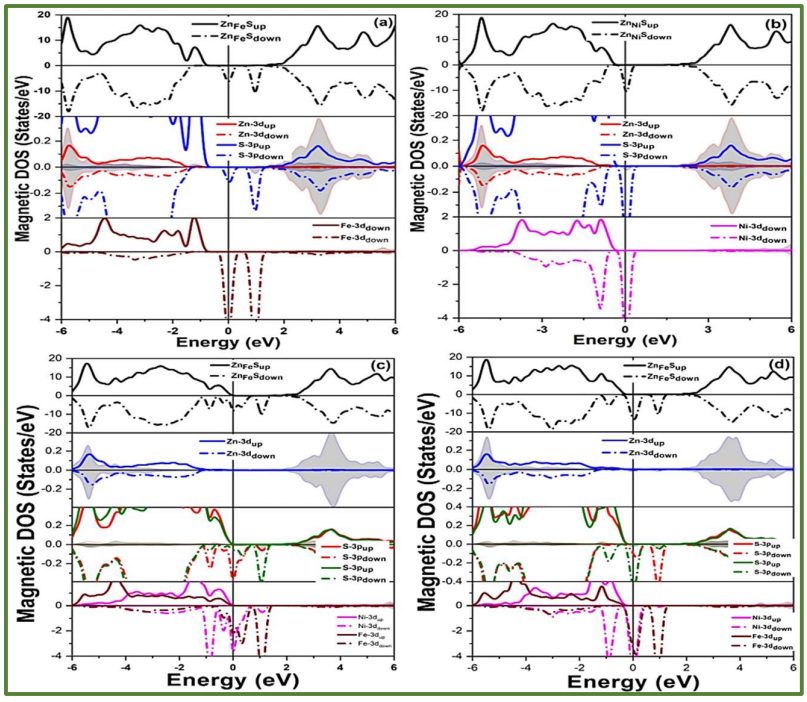

Fig 4.20 Spin polarized density of states for (a) ZnFeS, (b) ZnNiS, (c) $Zn_{Fe,Ni}S_{Int}$ and (d) $Zn_{Fe,Ni}S_{Non\text{-}Int.}$

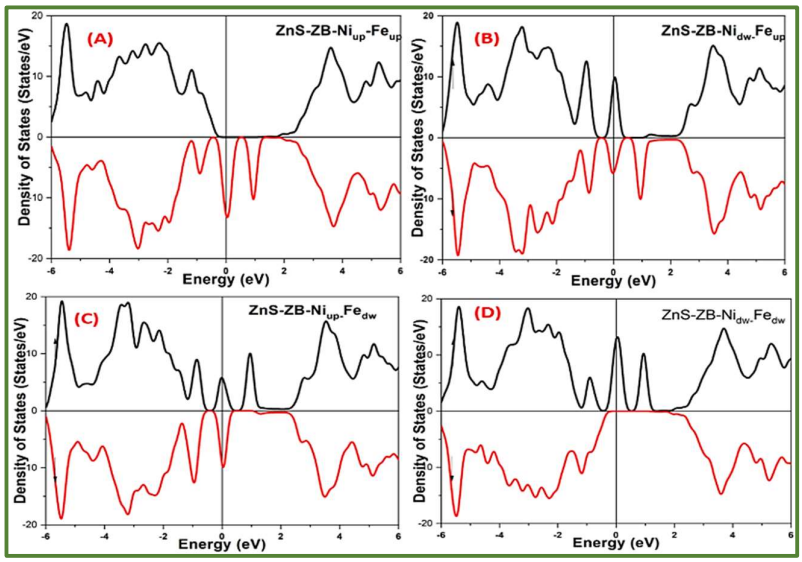

Fig. 4.21 The spin-dependent density of states (States/eV) for Ni, Fe doped, and co-doped ZnS, for non-interacting Fe-Ni with different spin polarization.

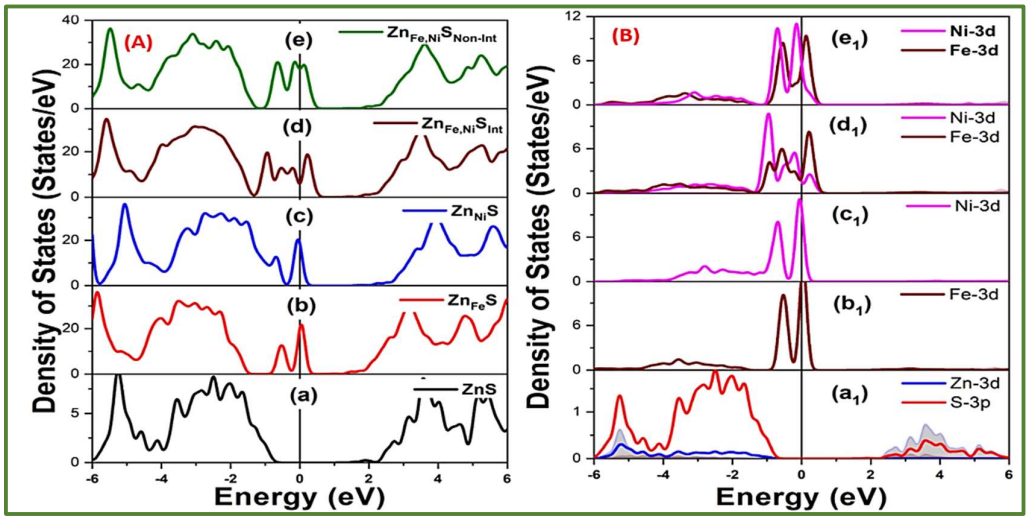

Fig. 4.22. Total and projected Density of states for (a) ZnS, (b) ZnFeS, (c) ZnNiS, (d) $Zn_{Fe,Ni}S_{Int}$ and (e) $Zn_{Fe,Ni}S_{Non-Int}$.

Localization of 3d orbitals, the shift of VB towards lower energy in $Zn_{Fe}S$, and 3p-3d hybridization of S-Ni towards VB in $Zn_{Ni}S$ are reported earlier by[32,42,43] Fe, Ni in $Zn_{Fe}S$, $Zn_{Ni}S$ respectively produce minority spin states in the forbidden region where, Fe and Ni show IB over E_F promoting themselves as half-metals and inclusion of ferromagnetic nature meanwhile, Ni activates the S-3p orbital resulting in indirect E_g in $Zn_{Ni}S$ from R-G, M-G as seen from Fig. 4.23 (a, b). Zn based on its electronegativity filled 3d orbital and states in the lower region maintain electronic neutrality.

The effective role of p_π-d_π interaction is visible in interacting and non-interacting $Zn_{Fe,Ni}S$ system from bands, and DOS, here Fe-S-Ni structural interaction in $ZnFe,_{Ni}S_{Int}$ leads to 3d-3p-3d orbital hybridization in the minority spin channel hence dispersed bands. This orbital coupling activates the M point in the momentum space for photogenerated charge carrier excitation with the influence of thermal energy because of its indirect nature. Charge channel formation regulates the effective charge separation, while in $Zn_{Fe,Ni}S_{Non\text{-}Int}$ separation between Fe-Ni keeps localization of orbitals in the forbidden region intact, although flat band curvature from M-G point results in the heavy hole which is beneficial for a reduced rate of recombination on the direct transition from VB-CB.

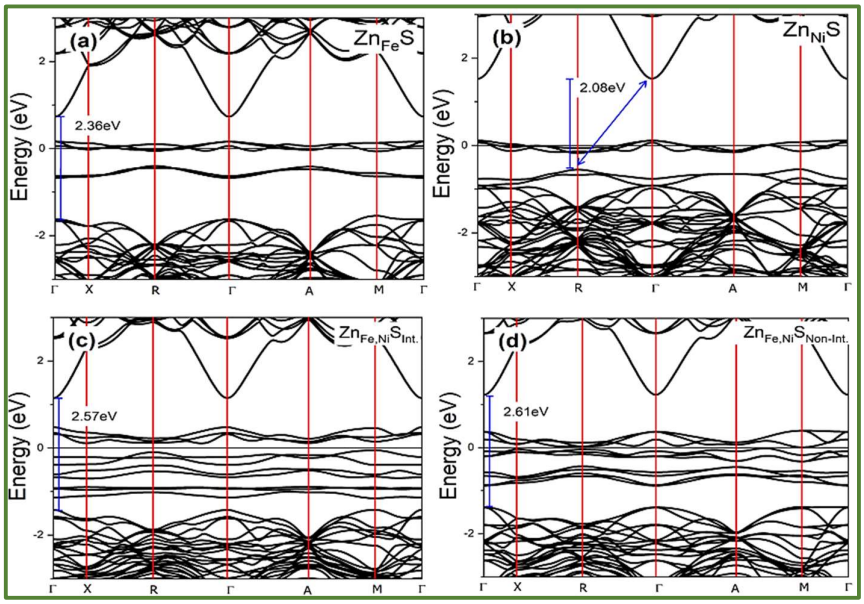

Fig. 4.23. Band structures with E_F shifted to 0.0 eV for (a) ZnFeS, (b) ZnNiS, (c) $Zn_{Fe,Ni}S_{Int}$ and (d) $Zn_{Fe,Ni}S_{Non\text{-}Int}$.

The impact of orbital interaction and localization affects the band curvature hence the electron-hole mobility and separation, here we have calculated the effective mass ratio (β) from the parabolic curve fitting method. The effective mass ratio describes the variance in the electron and hole effective mass and mobility hence the rate of recombination. Table. 1 shows the highest variance in pristine followed by $Zn_{Fe,Ni}S_{Non\text{-}Int}$ signifying an increase in recovery time of e^--h^+ pair and larger activity over the surface. Despite lower β than ZnS, $Zn_{Fe,Ni}S_{Non\text{-}Int}$ have deep trapping sites well localized over E_F for further degradation in the recombination rate providing a wide window range for surface assisted catalysis.

Further study of magnetic properties included calculation of magnetic moment and DOS with four spin configurations of Fe, Ni, where among Fe(↑)-Ni(↑)↓, Fe(↑)-Ni(↓), Fe(↓)-Ni(↑), and

Fe(↓)-Ni(↓), the configuration with Fe(↓)-Ni(↑) was found most stable (Table 4.10) with the magnetic moment of -0.135 μ_B/f.u. Atomic magnetic moment and spin-polarized PDOS shows strong localization of magnetic moment over Fe(3.01), Ni(1.21), Fe(3.05)-Ni(1.07), and Fe(3.11)-Ni(1.11) for $Zn_{Fe}S$, $Zn_{Ni}S$, $Zn_{Fe,Ni}S_{Int}$ and $Zn_{Fe,Ni}S_{Non\text{-}Int}$ respectively and uniform polarization of its neighbor S atom. This spin distribution induced confirms the role of p_π-d_π interaction in inducing ferromagnetic phenomenon in all the mono- and co-doped systems promising its application as a magnetically recycled photocatalyst.

Table 4.10 Calculated total energy and magnetic moments of $Zn_{0.88}Fe_{0.06}Ni_{0.06}S$ (non-interacting Fe-Ni).

S.No	Sample	Total Energy (Ry)	Magnetic Moment (μ_B/formula unit)
1.	$Zn_{0.88}Fe_{0.06}Ni_{0.06}S$ (Fe-up, Ni-up)	-2243.09934920 Ry	0.312 μ_B/f.u.
2.	$Zn_{0.88}Fe_{0.06}Ni_{0.06}S$ (Fe-up, Ni-dw)	-2243.09971744 Ry	0.135 μ_B/f.u.
3.	$Zn_{0.88}Fe_{0.06}Ni_{0.06}S$ (Fe-dw, Ni-up)	-2243.09971770 Ry	-0.135 μ_B/f.u.
4.	$Zn_{0.88}Fe_{0.06}Ni_{0.06}S$ (Fe-dw, Ni-dw)	-2243.09934922 Ry	-0.313 μ_B/f.u

Optical and Photocatalytic Property

Along with wide E_g, rapid migration of photo-generated charge carriers, reduced rate of recombination, and reusability of photocatalyst are the most important factor governing the generation of electron-hole pair by photo-excitation from VB to CB on optical absorbance. TM-3d orbitals of dopant have been found to induce trap sites which are known to increase the visible light absorption by increasing the absorption coefficient and introducing multiple pathways for transition increasing the probability of charge separation and providing a large number of chemical reaction activities. In Fig. 4.24 (a), the absorbance coefficient of ZnS is presented by the shaded region for reference, the area under the curve shows the highest absorbance by $Zn_{Fe,Ni}S_{Non\text{-}Int,}$ and $Zn_{Ni}S$, whereas Ni-doped-ZnS show higher absorption due to the formation of p-type semiconductor and $Zn_{Fe,Ni}S_{Non\text{-}Int}$ is a wide bandgap semiconductor with the localized 3d-3p intermediate state in the forbidden region.

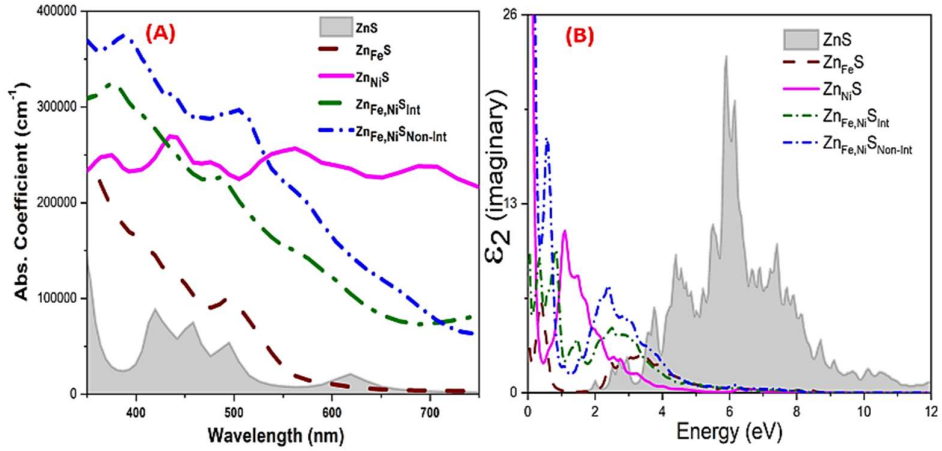

Figure 4.24. Absorption coefficient and imaginary part of dielectric function for ZnS, $Zn_{Fe}S$, $Zn_{Ni}S$, $Zn_{Fe,Ni}S_{Int}$ and $Zn_{Fe,Ni}S_{Non-Int}$.

Fig. 4.24(b) denotes the imaginary part of the dielectric function plotted against the energy, the peak visible at 2 eV for ZnS denotes its transition between sp-hybridized VB and CB. $Zn_{Fe}S$ and $Zn_{Ni}S$ display low energy peaks relating to their transition from VB-IB and high energy peak corresponding to the transition from IB-CB as seen in the band structure for the respective structure. The presence of two distinguished peaks at low energy and another around 2.5eV in $Zn_{Fe,Ni}S_{Non-Int}$ verify the presence of localized IB while dispersed peaks in $Zn_{Fe,Ni}S_{Int}$ in low energy region denotes partial p_{π}-d_{π} coupling while broad peak represents dispersed IB. Optical property study helps to understand the modification to be done in photocatalyst for improving its charge separation and increasing recovery time, here the modification describes efficient enhancement in both.

A study performed over the photocatalytic reduction and oxidation mechanism directs us towards the role of band edges in the overall investigation of the redox potential of the material. Investigation of ZnS for photocatalytic activity is limited to its bandgap, charge carrier mobility, absorption, and dye degradation. Here, we have calculated the band edge for pristine-ZnS, $Zn_{Fe}S$, $Zn_{Ni}S$, $Zn_{Fe,Ni}S_{Int}$ and $Zn_{Fe,Ni}S_{Non-Int}$ shown in Table. 8 and Fig. 4.25 using absolute electronegativity and E_g, band edge straddling by photocatalyst is prerequisite for reduction and oxidation reaction and here all samples seem to show potential for a redox reaction, while the large difference between E_v-$E_{oxidation}$, E_c-$E_{reduction}$ for $Zn_{Fe,Ni}S_{Int}$ and $Zn_{Fe,Ni}S_{Non-Int}$ predicts overcoming reaction energy barrier for overall water splitting.

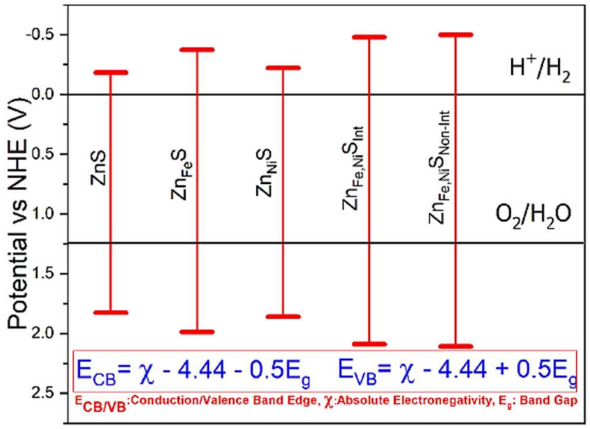

Fig. 4.25 Band edges along for ZnS, $Zn_{Fe}S$, $Zn_{Ni}S$, $Zn_{Fe,Ni}S_{Int}$ and $Zn_{Fe,Ni}S_{Non\text{-}Int}$ plotted against normal hydrogen electrode (NHE) potential.

4.5 Conclusion

In this study Fe-mono-doped, Ni-mono-doped, and Fe-Ni co-doped ZnS photocatalyst have been successfully synthesized and characterized by X-ray powder diffraction, EDS analysis, FESEM, HRTEM analysis, and surface area by BET, the surface charge was estimated by Zeta potential, and the magnetic study was done by using RT VSM instrument. An electrochemical study was carried out to know the charge densities and redox behaviour of all photocatalysts. After the synthesis of the material, their photocatalytic activity was estimated under UV HPMV lamp for rhodamine dye degradation. The synergistic effect between Fe-Ni co-doped ZnS with sulfur-vacancy defects is responsible for the enhanced photocatalytic activity and stability. Efficient charge transfer and reserved electron-hole recombination are obtained at the interface of the Fe-Ni co-doped ZnS leads to higher photocatalytic activity.

Photocatalytic experiment

600 mL of an aqueous solution of RhB (13.207 µM, 6.32 ppm) was mixed with 10 mg synthesized NPs at RT, pH 6.5, and thoroughly mixed in dark for 60 min. Subsequently, the mixture was transferred to the photoreactor. At every 10 min, the sampling (2.5mL) of the irradiated solution was carried out for up to 320min. In the end, the solution was centrifuged at 6000 rpm to recover the catalyst and the concentration of RhB present in the solution was determined by using UV absorption spectroscopy.

the PL spectra of illuminated basic solution of terephthalic acid (5×10^{-4} M terephthalic in 2×10^{-3} M NaOH) in presence of $Zn_{1-0.10}Fe_{0.05}Ni_{0.05}S$ doped ZnS NPs at different time intervals were recorded (Fig. 6B). The PL intensity at 425 nm increases with irradiation time in presence of

$Zn_{1-0.10}Fe_{0.05}Ni_{0.05}S$ co-doped ZnS NPs. This observation confirms that $^{\bullet}OH$ actively takes part in the degradation of RhB dye in an aqueous solution.

4.6 References

(1) Shirzadi, H.; Nezamzadeh-Ejhieh, A. An Efficient Modified Zeolite for Simultaneous Removal of Pb(II) and Hg(II) from Aqueous Solution. *J. Mol. Liq.* **2017**, *230*, 221–229.

(2) Hama Aziz, K. H.; Miessner, H.; Mueller, S.; Mahyar, A.; Kalass, D.; Moeller, D.; Khorshid, I.; Rashid, M. A. M. Comparative Study on 2,4-Dichlorophenoxyacetic Acid and 2,4-Dichlorophenol Removal from Aqueous Solutions via Ozonation, Photocatalysis and Non-Thermal Plasma Using a Planar Falling Film Reactor. *J. Hazard. Mater.* **2018**, *343*, 107–115.

(3) Anari-Anaraki, M.; Nezamzadeh-Ejhieh, A. Modification of an Iranian Clinoptilolite Nano-Particles by Hexadecyltrimethyl Ammonium Cationic Surfactant and Dithizone for Removal of Pb(II) from Aqueous Solution. *J. Colloid Interface Sci.* **2015**, *440*, 272–281.

(4) Salimi, F.; Emami, S. S.; Karami, C. Removal of Methylene Blue from Water Solution by Modified Nano-Boehmite with Bismuth. *Inorg. Nano-Met. Chem.* **2018**, *48*, 31–40.

(5) Nasrollahzadeh, M.; Issaabadi, Z.; Sajadi, S. M. Green Synthesis of a Cu/MgO Nanocomposite by Cassytha Filiformis L. Extract and Investigation of Its Catalytic Activity in the Reduction of Methylene Blue, Congo Red and Nitro Compounds in Aqueous Media. RSC Adv. **2018**, 8, 3723-3735.

(6) Zhang, H.; Xue, G.; Chen, H.; Li, X. Magnetic Biochar Catalyst Derived from Biological Sludge and Ferric Sludge Using Hydrothermal Carbonization: Preparation, Characterization and Its Circulation in Fenton Process for Dyeing Wastewater Treatment. *Chemosphere* **2018**, *191*, 64–71.

(7) Li, Y.; Guo, S.; Yang, H.; Chao, Y.; Jiang, S.; Wang, C. One-Step Synthesis of Ultra-Long Silver Nanowires of over 100 Mm and Their Application in Flexible Transparent Conductive Films. RSC Adv. **2018**, 8, 8057-8063.

(8) Ikram, M.; Tabassum, R.; Qumar, U.; Ali, S.; Ul-Hamid, A.; Haider, A.; Raza, A.; Imran, M. Promising Performance of Chemically Exfoliated Zr-Doped MoS 2 Nanosheets for Catalytic and Antibacterial Applications. *RSC Adv.* 2020,10, 20559-20571.

(9) Ikram, M.; Khan, M. I.; Raza, A.; Imran, M.; Ul-Hamid, A.; Ali, S. Outstanding Performance of Silver-Decorated MoS2 Nanopetals Used as Nanocatalyst for Synthetic Dye Degradation. *Physica E Low-Dimens. Syst.* **2020**, *124,*114246.

(10) Raza, A.; Ikram, M.; Aqeel, M.; Imran, M.; Ul-Hamid, A.; Riaz, K. N.; Ali, S. Enhanced Industrial Dye Degradation Using Co-Doped in Chemically Exfoliated MoS2 Nanosheets. *Appl. Nanosci.* **2020**, *10*, 1535–1544.

(11) Bahrami, M.; Nezamzadeh-Ejhieh, A. Effect of the Supported ZnO on Clinoptilolite Nano-Particles in the Photodecolorization of Semi-Real Sample Bromothymol Blue Aqueous Solution. *Mater Sci Semicond Process.* **2015**, *30*, 275–284.

(12) Zhang Junwei, J.; Fu Dafang, D.; Xu, Y.; Liu, C. Optimization of Parameters on Photocatalytic Degradation of Chloramphenicol Using TiO_2 as Photocatalyist by Response Surface Methodology. *J. Environ. Sci.* **2010**, *22*, 1281–1289.

(13) Kaneko, S.; Watanabe, S.; Kasai, S.; Nishino, T.; Tsukagoshi, K.; Kiguchi, M. Near-

Infrared-Light-Induced Decomposition of Rhodamine B Triggered by Localized Surface Plasmon at Gold Square Dimers with Well-Defined Separation Distance. *AIP Adv.* **2019**, *9*, 35153.

(14) Shahwan, T.; Abu Sirriah, S.; Nairat, M.; Boyaci, E.; Eroĝlu, A. E.; Scott, T. B.; Hallam, K. R. Green Synthesis of Iron Nanoparticles and Their Application as a Fenton-like Catalyst for the Degradation of Aqueous Cationic and Anionic Dyes. *Chem. Eng. J.* **2011**, *172*, 258–266.

(15) Neppolian, B.; Choi, H. C.; Sakthivel, S.; Arabindoo, B.; Murugesan, V. Solar/UV-Induced Photocatalytic Degradation of Three Commercial Textile Dyes. *J. Hazard. Mater.* **2002**, *89*, 303–317.

(16) Shams-Ghahfarokhi, Z.; Nezamzadeh-Ejhieh, A. As-Synthesized ZSM-5 Zeolite as a Suitable Support for Increasing the Photoactivity of Semiconductors in a Typical Photodegradation Process. *Mater. Sci. Semicond. Process.* **2015**, *39*, 265–275.

(17) Guettaï, N.; Ait Amar, H. Photocatalytic Oxidation of Methyl Orange in Presence of Titanium Dioxide in Aqueous Suspension. *Desalination* **2005**, *185*, 427–437.

(18) A.Fujishima, K. H. Electrochemical Photolysis of Water at a Semiconductor Electrode. *Nat. new biol.* **1972**, *240*, 226–229.

(19) Chandrasekaran, S.; Yao, L.; Deng, L.; Bowen, C.; Zhang, Y.; Chen, S.; Lin, Z.; Peng, F.; Zhang, P. Recent Advances in Metal Sulfides: From Controlled Fabrication to Electrocatalytic, Photocatalytic and Photoelectrochemical Water Splitting and Beyond. *Chem. Soc. Rev* **2019**, *48*, 4178–4280.

(20) Shah, E.; Vaghasiya, J. V.; Soni, S. S.; Panchal, C. J.; Suryavanshi, P. S.; Chavda, M.; Soni, H. P. Ni Doped ZnS Nanoparticles as Photocatalyst: Can Mixed Phase be Optimized for Better Performance? *J. Environ. Chem. Eng.* **2016**, *4*, 4708–4718.

(21) Sreenivasulu, B.; Reddy, S. V.; Reddy, P. V. Synthesis and Properties of (Co , Ni) Co-Doped ZnS Nanoparticles. *J. Nanotechnol Material Sci.* **2017**, 4, 1–18.

(22) Harish, G. S.; P, S. R. Synthesis and Characterization of Ce , Cu Co-Doped ZnS Nanoparticles. *Physica B Condensed Matter.* **2015**, *473*, 48–53.

(23) Dixit, N.; Vaghasia, J. V.; Soni, S. S.; Sarkar, M.; Chavda, M.; Agrawal, N.; Soni, H. P. Photocatalytic Activity of Fe Doped ZnS Nanoparticles and Carrier Mediated Ferromagnetism. *J. Environ. Chem. Eng.* **2015**, *3*, 1691–1701.

(24) Patterson, A. L. The Scherrer Formula for X-Ray Particle Size Determination. *Phy.Rev.* **1967**, *56*, 5–24.

(25) Mote, V.; Purushotham, Y.; Dole, B. Williamson-Hall Analysis in Estimation of Lattice Strain in Nanometer-Sized ZnO Particles. *J. Theor. Appl. Phys.* **2012**, *6*, 2–9.

(26) Rossetti, R.; Hull, R.; Gibson, J. M.; Brus, L. E. Excited Electronic States and Optical Spectra of ZnS and CdS Crystallites in the ≈15 to 50 Å Size Range: Evolution from Molecular to Bulk Semiconducting Properties. *J. Chem. Phys.* **1985**, *82*, 552–559.

(27) Tauc, J. Optical Properties and Electronic Structure of Amorphous Ge and Si. *Mater. Res. Bull.* **1968**, *3*, 37–46.

(28) Sharma, M.; Jain, T.; Singh, S.; Pandey, O. P. Photocatalytic Degradation of Organic

Dyes under UV–Visible Light Using Capped ZnS Nanoparticles. *Sol. Energy* **2012**, *86*, 626–633.

(29) Devi, R.; Raveendran, R.; Vaidyan, A. V. *Synthesis and Characterization of Mn^{2+}-Doped ZnS Nanoparticles*. J. phys. 2007, 68, 679-687.

(30) Murugadoss, G.; Ramasamy, V. Synthesis, Effect of Capping Agents and Optical Properties of Manganese-Doped Zinc Sulphide Nanoparticles. *Luminescence* **2013**, *28*, 69–75.

(31) Rodríguez, S.; Zandalazini, C.; Navarro, J.; Vadiraj, K. T.; Albanesi, E. A. First Principles Calculations and Experimental Study of the Optical Properties of Ni-Doped ZnS. *Mater. Res. Exp.* **2019**, *7*, 016303.

(32) Mahmood, Q.; Hassan, M.; Noor, N. A. Theoretical Study of Electronic, Magnetic, and Optical Response of Fe-Doped ZnS: First-Principle Approach. *J. Supercond. Nov. Magn.* **2017**, *30*, 1463–1471.

(33) Wan, H.; Xu, L.; Huang, W. Q.; Huang, G. F.; He, C. N.; Zhou, J. H.; Peng, P. Band Engineering of ZnS by Codoping for Visible-Light Photocatalysis. *Appl. Phys. A: Mater. Sci. Process.* **2014**, *116*, 741–750.

(34) Hommel, D.; Hartmann, H.; Busse, W.; Gumlich, H. E.; Kreissl, J. II–VI Compounds Codoped with Transition Metals and Rare Earths: ZnS:Mn^{2+},Sm^{3+} Bulk Crystals Site Selection and Energy Transfer. *J. Lumin.* **1991**, *48–49*, 655–660.

(35) Boyn, R.; Muller, S.; Dziesiaty, J.; Zimmermann, H. Ho Centres in ZnS in the 3+ and 2+ State Studied by Optical and Electron Paramagnetic Resonance Spectroscopy. *J. Phys. Condens. Matter* **1995**, *7*, 9061–9073.

(36) Li, D.-F.; Luo, M.; Li, B.-L.; Wu, C.-B.; Deng, B.; Dong, H.-N. Low-Resistivity p-Type Doping in Wurtzite ZnS Using Codoping Method. *Adv. Condens. Matter Phys.* **2013**, 4, 1-4.

(37) Gaa, I. E.; Hohenbergt Ecole, P.; Superzeure, I'aris, X.; And, F.; Konnt, W. Inhomogeneous Electron Gas *Phys. Rev*. **1964**, 136, 865.

(38) Kohn, W.; Sham, L. J. *Self-Consistent Equations Including Exchange and Correlation Effects*. *Phys. Rev*. **1965,** 140, 1134.

(39) Giannozzia, P.; Andreussib, O.; Brummec, Bunaud, I, T. O.; Buongiorno Nardellie, M. M.; Calandrad, R.; Carf, C.; Cavazzonig, D.; Ceresolih, M. C. et al. Advanced Capabilities for Materials Modelling with Quantum Espresso. *Mater. Res. Exp.* **2019**, 0–12.

(40) Perdew, J. P.; Burke, K.; Ernzerhof, M. Generalized Gradient Approximation Made Simple. *Phy. Rev. Lett.* **1996**, *77*, 3865–3868.

(41) S. Ves, * U. Schwarz, N. E. Christensen, K. Syassen, and M. C. Cubic Zns under Pressure: Optical-Absorption Edge, Phase Transition, and Calculated Equation of State. *Phys. Rev. B* **2014**, *42*, 9113–9118.

(42) Saikia, D.; Borah, J. P. Investigations of Doping Induced Structural, Optical and Magnetic Properties of Ni Doped ZnS Diluted Magnetic Semiconductors. *J. Mater. Sci.: Mater. Electron.* **2017**, *28*, 8029–8037.

(43) Xiao, W. Z.; Wang, L. L.; Rong, Q. Y.; Xiao, G.; Meng, B. Magnetism in Undoped ZnS Studied from Density Functional Theory. *J. Appl. Phys.* **2014**, *115, 213905.*